Semi-analytical model of noise transmission through finite length cylinder with poroelastic core using Biot's and Shell theories

Fares Naccache, Mohamed-Ali Hamdi, Jean-Daniel Chazot, Marc Anciant

Journal of Sound and Vibration 535 (2022) 117102

Contents lists available at ScienceDirect

Journal of Sound and Vibration

journal homepage: www.elsevier.com/locate/jsvi

Semi-analytical model of noise transmission through finite length cylinder with poroelastic core using Biot's and Shell theories

Fares Naccache [a,*], Mohamed-Ali Hamdi [a], Jean-Daniel Chazot [a], Marc Anciant [b]

[a] Laboratoire Roberval, Université de Technologie de Compiègne, Centre de Recherches de Royallieu, CS 60319, 60203, Compiègne Cedex, France
[b] Engineering Systems International, F-60200 Compiègne, France

ARTICLE INFO

Keywords:
Sound transmission
Noise reduction
Vibroacoustics
Finite length cylinder
Biot's theory
Porous material

ABSTRACT

In the open literature, sound transmission through cylindrical structures is often considered for infinitely long cylinders for which full analytical solutions can be derived. However, when dealing with finite cylinders subjected to arbitrary boundary conditions, establishing a general analytical solution is more complex to achieve and appropriate resolution techniques should be used. In the present study, a consistent semi-analytical model of sound transmission through such finite length and multilayered cylinders is presented. The orthotropic shell is modeled with 2D first order shear deformation theory and the poroelastic core is modeled with full 3D Biot's theory in u-p format. Analytical expressions are used for the acoustic domains while closed form Rayleigh–Ritz expansion and 1D finite element method are used for the structural domains. Results are validated with those of literature and those given by full numerical simulations. Furthermore, the effect of structural and acoustical resonances on noise transmission are discussed through finite/infinite cylinders superposition and with respect to angle of incidence and porous layer thickness. The contribution of internal resonances demonstrates the importance of the cylinder finiteness for oblique incidences.

1. Introduction

Acoustic isolation is of a great importance in aeronautic and aerospace industries. In fact, structures are designed to be lightweight and composite materials are widely used in order to increase payload capacities and decrease launch costs. However, such designs make these structures acoustically transparent and hence it deteriorates sound transmission loss (STL) performances. One passive way to improve acoustic performances and reduce noise transmission is the use of poroelastic materials as an acoustic protection. Poroelastic materials are known to be efficient in absorbing acoustic waves while having low mass density. This research work focuses on sound transmission through cylindrical structures incorporating porous layers.

Studies on STL through cylindrical structures have been using two main approaches to model the porous liners : equivalent fluid models and full 3D Biot's theory [1,2]. Equivalent fluid models consider the porous medium as a fluid medium modified by the presence of the skeleton. In this approach, there are two classical models : rigid frame model and limp model. The former considers rigid and motionless skeleton while the latter considers the inertial effect of a rigid skeleton. Another fluid equivalent model is the *simplified method* proposed by Lee et al. [3]. Based on the work of Bolton et al. [4] who developed a method (known as *the full method*) for the analysis of the sound transmission through flat panels with porous material using Biot's theory, the *simplified method* [3] consists of comparing the energies of the three waves propagating in a poroelastic material, two longitudinal

* Corresponding author.
E-mail address: fares.naccache@utc.fr (F. Naccache).

https://doi.org/10.1016/j.jsv.2022.117102
Received 26 January 2022; Received in revised form 15 May 2022; Accepted 7 June 2022
Available online 16 June 2022

waves and one rotational wave, and then keeping the strongest one between them as the only wave propagating in an equivalent fluid medium. Many authors [5–8] used this simplified model in their STL investigations. Biot's theory [1,2] is a more complete framework to model sound propagation through porous media. It considers an elastic frame fully saturated with a fluid and their mutual physical interactions. Biot's theory has been used in STL studies through infinite cylinders [9–13].

Literature review on STL through cylindrical structures shows that most of the published works consist of models established for infinitely long cylinders while only fewer works consider finite cylinders, see for example the review given by Zarastvand et al. [14]. This gap can be mainly explained by an easier access to the exact and full analytical solutions when considering infinite cylinders. For instance, see the works of Magniez et al. [13,15] where the layers of the cylinder are modeled with 2D shell theory, 3D elastic theory and 3D Biot's theory and where the analytical solution is derived using the Transfer Matrix Method. However, when dealing with finite cylinders subjected to arbitrary boundary conditions, establishing a general analytical solution is more complex to achieve and approximation techniques are used such as power series expansion, trigonometric Rayleigh–Ritz or Fourier expansions [16–20].

Numerical resolution methods such as Finite Element Method (FEM) and Boundary Element Method (BEM) represent an alternative to analytical approaches. The main advantage of these methods is their capacity to adapt to complex geometries and consider arbitrary boundary conditions. Works such in [21,22] investigated cylindrical structures lined with porous materials modeled with Biot's theory using FEM. Other techniques such as Wave and Finite Element Methods were used in Ref [23] to analyze sound transmission and sound radiation of infinitely long cylinder subjected to arbitrary internal or external excitation, and recently the Generalized Differential Quadrature Method was used in [24] to study the vibrational response of porous truncated conical shells.. Nonetheless, in order to ensure an acceptable accuracy in full numerical methods, the use of a minimum number of elements per wavelength is mandatory. Due to this high computational cost when it comes to higher frequency range, analytical models remain more convenient for lighter and faster parametric studies at the design stages.

Statistical Energy Analysis (SEA) is an energy-based method where analytical approaches are used. In contrast to deterministic analysis, SEA is a probabilistic way to study the dynamic response where the structure is decomposed into subsystems characterized by its modal energy densities and the principle of conservation of energy flow is satisfied. These assumptions make the SEA approach valid in high frequency domain where the modal densities are high enough [25]. One can cite among the early works those of White [26] and Pope [27] who considered STL through finite cylinders. White [26] presented an energy averaging approach based on gross quantities such as modal density, joint acceptance and cylinder and cavity resistances to estimate sound transmission through a thin cylindrical shell and compared the analytical results in frequency band with the experimental measurements. Pope [27] investigated sound transmission into a closed cylinder and a rectangular parallelepiped enclosure under reverberant acoustic fields using SEA. The effects of resonant and non-resonant shell modes on sound transmission are examined and results are compared to experimental measurements. Yuan et al. [28] compared STL of a fuselage modeled as a finite length cylindrical shell using FE, SEA and hybrid FE-SEA methods. It is found that the cylinder length has little influence on the sound insulation. Oliazadeh et al. [29] developed an analytical model of the vibro-acoustic response of a finite length cylindrical shell based on SEA and carried out STL measurements (from the inside to the outside of the shell) based on two experimental methods. Noise Reduction and Transmission Loss factors are calculated and the effects of the presence of fiberglass material are investigated. The comparison between the theoretical and experimental results shows good agreements. Recently, Gupta and Parey [30] developed a SEA-based analytical model of sound transmission of cylindrical acoustic enclosures. The model includes the resonant as well as the non-resonant wave responses. The results are compared to experimental ones and a good agreement is observed.

The dynamic behavior of infinitely long cylinders differ from those of finite cylinders and hence their vibro-acoustic responses and STL performances should differ as well, particularly in the low frequency range (long wavelengths) in which the boundary conditions become more significant as portrayed in Ref. [31] for example. In facts, the nature of waves changes whether the medium is unbounded or bounded. In the former, the elastic cylinder is subjected to axial traveling waves while in the latter it is subjected to standing waves, and so is the case of the acoustic waves in the internal fluid as well. It appears that the main difference between the finite and infinite STL modelings consists in the contribution of the structural and acoustical resonances, namely the axial resonances. Note that the effects of radial resonances have been studied by Koval [32] for infinitely long cylindrical shell and it has been found that for a non-resonant cavity the Noise Reduction (NR) index follows the same pattern as the Transmission Loss (TL) index, and for a resonant cavity the NR index exhibits wide fluctuations and a general level decrease.

Considering STL through finite length cylinders, Lesueur presented in his book [33] two vibro-acoustic models for finite thin isotropic simply-supported shell : the first model is based on strong fluid–structure coupling conditions while the second model uses weak coupling conditions and modal projection. It is shown that for light fluid both models are in a good agreement. Li and Vipperman [34] developed an analytical model for sound transmission through finite thin cylinder. The external pressure field is approximated using the infinite cylinder expression for plane wave excitation while the interior pressure field is approximated using rigid-wall acoustic cavity modal projection. Cylinder motion is modeled with Donnel-Mushtari and Flugge's theories and the vibro-acoustic problem is derived using modal-interaction approach. A revised NR index expression for finite length cylinder similar to TL index expression for infinite cylinder is proposed. Results are compared with experimental data for a Chamber Core and effects of acoustic damping are investigated. Hosseini-Toudeshky et al. [35] presented a semi-analytical model for STL through finite thick isotropic cylinder. Using the solution developed in [36], the cylinder displacement field is obtained through Helmoltz decomposition in conjunction with separation of variables; and the boundary conditions are split into two parts : one part is satisfied exactly while the other part is satisfied using orthogonalization technique. Noise reduction of the cylinder is evaluated for plane wave excitation and for monopole and dipole radiations with different positions. Effects of boundary conditions and cylinder length are investigated. Zhou et al. [37] extended their previous work and considered sound transmission through double cylindrical thin shells with finite length and lined with porous material under turbulent boundary layer excitation. The solution is expanded into a double series using

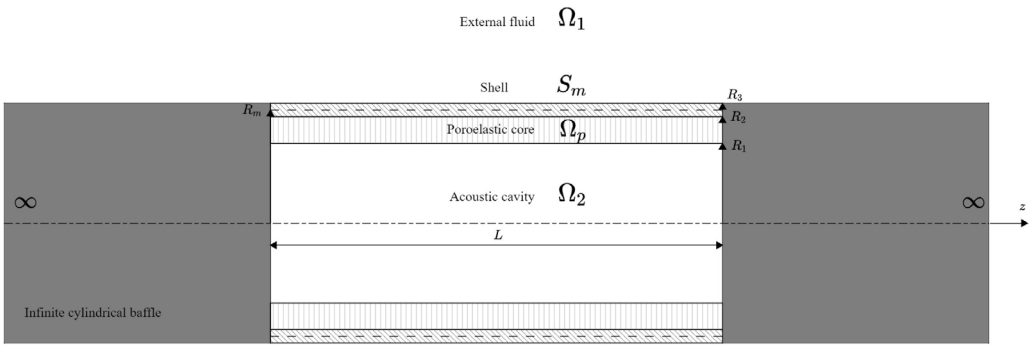

Fig. 1. Problem geometry and physical domains : a finite length elastic cylinder mounted on infinite length cylindrical baffles.

cylindrical harmonics and Rayleigh–Ritz approximation; and the turbulent boundary layer is modeled using both Corcos model and Efimtsov model. The sound level inside the cylinder is therefore evaluated using the power spectral density of the kinetic energy of the inner shell and the power spectral density of the pressure fluctuation due to the excitation. Results are compared for different boundary configurations of the core and the effects of air gaps and porous material are also investigated. Recently, Darvish Gohari et al. [20] proposed an analytical model for STL through simply-supported double walled cylinder sandwiching a porous core. The shells are modeled with first order shear deformation theory and the core is modeled with Biot's theory using u-U formulation. In this work, it is declared that the solution is expanded into double Fourier series in the circumferential and longitudinal directions. Moreover, the wave propagation through the porous layer is described with Helmoltz decomposition of the displacement fields. The inner shell is assumed to be totally absorbent, hence the transmitted pressure in the finite acoustic cavity consists of inward traveling waves in the radial direction and the sound level in the cavity is evaluated with TL index. The effect of geometrical parameters are investigated and results are compared with those given by infinite cylinder. Golzari and Jafari [19] presented an analytical model of STL through truncated circular conical shell subjected to arbitrary boundary conditions and impinged by an incident plane wave. Love's theory is used to model the isotropic conical shell and a convergent power series solution is used to obtain the analytical expression of shell displacement. Thus, recurrence relations are obtained for the power series coefficients and the convergence is demonstrated. Moreover, the acoustic fields interacting on the conical shell are locally approximated with the expressions of sound pressures interacting with cylindrical shell. Assuming a non-resonant cavity, the STL is evaluated using the TL index. In [38], Golzari and Jafari used the same resolution techniques as in [19] and extended their works by incorporating a porous liner and using a double-walled truncated conical shell. The *simplified method* [3] is used to describe the wave propagation within the poroelastic material. The proposed model is first validated with analytical and experimental results in the special case of cylindrical shell and it is observed that by increasing the shell length, the STL tends to those of infinite shell. Then, the influence of the problem parameters on STL such as shell geometrical and physical properties, shell axial boundary condition and porous liner boundary conditions and thickness, angle of incidence and surrounding fluid properties are investigated. It is found that the boundary constraints are more important in the low frequency region rather than high frequency region, and the position of the first ring frequency is affected by the boundary condition type. The STL in the stiffness controlled region can be enhanced either by increasing shell thickness, reducing shell radius or shell length. Using a heavier fluid (from air to water), the STL decreases at low and middle frequencies whereas it increases at high frequencies; besides the acoustic resonances are eliminated. The poroelastic liner improves the STL in all frequency ranges except at low frequencies, and this improvement increases with the thickness of the liner. Moreover, an air gap separating the liner and the facing shell improves the STL above the first ring frequency.

The present study proposes a consistent semi-analytical model of sound transmission through finite length multilayered cylinders impinged by incident plane waves. The orthotropic shell is modeled with 2D First-order Shear Deformation Theory (FSDT) and the poroelastic core is modeled with full 3D Biot's theory expressed in u-p format. Analytical expressions are used for the acoustic pressures in the internal and external fluid domains and closed form Rayleigh–Ritz expansion is used to ensure the structural boundary conditions. Furthermore, 1D finite element method is used to describe the wave propagation through the porous core thickness. The global vibro-acoustic problem is solved in a weak form and an analytical expression of Noise Reduction index is presented. After results validation with those of literature and those given by full numerical simulations, the contribution of the internal resonances in the noise insulation at low and mid frequency regions are discussed through finite/infinite superposition regarding to angle of incidence and porous layer thickness. Results show that the proposed model can be effectively used to compute sound transmission through cylindrical structures coupled with external lightweight fluids.

2. Modeling and assumptions of the vibro-acoustic problem

Consider a hollow cylinder with finite length L mounted on two rigid semi-infinite cylindrical baffles as depicted in Fig. 1. The cylinder is composed of an orthotropic shell lined with an isotropic poroelastic coating. The cylinder is surrounded by two fluids media in the exterior domain Ω_1 and interior domain Ω_2. A plane sound wave impinges the cylinder obliquely. It is worth

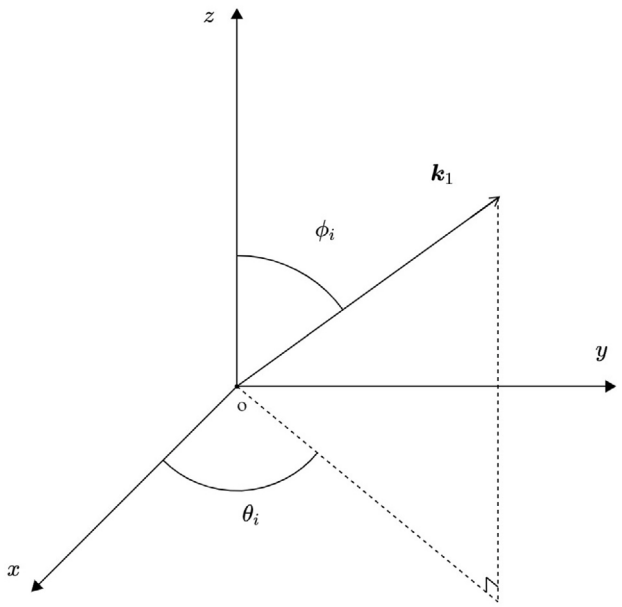

Fig. 2. Incident plane wave vector.

mentioning here that this configuration is not a limitation of the model and it has been considered for convenience and clarity of the presentation. The proposed methodology remains valid for other multilayered cylinder configurations such as double or triple walled structures lined with different materials.

For the study of sound transmission through the cylinder, the following assumptions are made:

- The study is under the classical linear vibroacoustics framework: linear elastic structures surrounded by ideal inviscid barotropic fluids;
- Variable separation technique is used;
- Time-dependent variables are assumed to be harmonic with $e^{-\mathrm{j}\omega t}$ time convention, where $\mathrm{j}^2 = -1$ is the imaginary number, ω the excitation angular frequency and t the time. In the rest of the article, time-dependence notation will be omitted;
- The pressure radiated by the vibrating elastic cylinder in the external fluid domain Ω_1 is neglected and hence the total external acoustic pressure is reduced to the incident and the diffracted waves. This assumption is valid for lightweight external fluid coupled with stiff cylinder.

3. Pressure fields in fluid domains

3.1. Pressure field in the external domain

The fluid properties in the exterior domain Ω_1 are the density and the speed of sound denoted by ρ_1 and c_1 respectively. The external pressure p_1 is assumed to be the sum of the incident plane wave pressure p_i and the wave pressure scattered by the rigid infinite cylinder noted $p_{s\infty}$, while neglecting the radiated pressure, such that:

$$p_1 = p_i + p_{s\infty} \tag{1}$$

The plane wave is incident at angles (ϕ_i, θ_i) and the corresponding wave vector $\boldsymbol{k}_1$ is given in the Cartesian coordinate system as shown in figure Fig. 2 (vectors and matrices are noted with bold symbols):

$$k_{1x} = \frac{\omega}{c_1} \sin(\phi_i) \cos(\theta_i) \tag{2a}$$

$$k_{1y} = \frac{\omega}{c_1} \sin(\phi_i) \sin(\theta_i) \tag{2b}$$

$$k_{1z} = \frac{\omega}{c_1} \cos(\phi_i) \tag{2c}$$

Using cylindrical coordinate system, one can show that expanding the incident plane wave in cylindrical harmonics gives:

$$p_i(r, \theta, z) = A_i \sum_{n=0}^{\infty} \epsilon_n \, \mathrm{j}^n J_n(k_{1r} r) \cos\left(n(\theta - \theta_i)\right) e^{\mathrm{j}k_{1z} z} \tag{3}$$

where A_i is the magnitude of the incident wave (and generally it is equal to unity), $\varepsilon_n = \begin{cases} 1 & \text{if } n = 0 \\ 2 & \text{if } n \geq 1 \end{cases}$ the Neumann factor, J_n the Bessel function of first kind and order n and $k_{1r} = \frac{\omega}{c_1} \sin(\phi_i)$ the radial wave number in the exterior domain Ω_1. Note the azimuthal argument in the cylindrical expansion $(\theta - \theta_i)$ is determined from the incident angle θ_i.

The scattered field by a rigid cylinder with infinite length $p_{s\infty}$ corresponds to outward traveling cylindrical waves and satisfying Sommerfeld radiation condition. These waves are expanded in cylindrical harmonics as follows:

$$p_{s\infty}(r,\theta,z) = \sum_{n=0}^{\infty} S_n H_n(k_{1r} r) \cos\left(n(\theta - \theta_i)\right) e^{\mathrm{j}k_{1z}z} \tag{4}$$

where S_n is the magnitude of order n and H_n is the Hankel function of first kind and order n defined by $H_n = J_n + \mathrm{j}Y_n$ with Y_n the Bessel function of second kind and order n. A reminder here about the temporal convention $e^{-\mathrm{j}\omega t}$ is given to highlight the expression of the scattered field $p_{s\infty}$ in terms of Hankel function of first kind.

For the rigid body problem, the radial component of the fluid displacement vector should vanish at the outer surface of the rigid cylinder:

$$\frac{1}{\rho_1 \omega^2} \nabla p_1 . \vec{e}_r = 0 \qquad \text{on } r = R_3 \tag{5}$$

where ∇ is the gradient operator, $\frac{1}{\rho_1\omega^2}\nabla p_1$ the fluid displacement vector according to Euler relation and $(\vec{e}_r, \vec{e}_\theta, \vec{e}_z)$ the cylindrical basis vectors.

Using the expressions in Eqs. (1), (3), (4) and satisfying the boundary condition Eq. (5) yield to the expression of the scattered magnitude S_n:

$$S_n = -A_i \varepsilon_n \mathrm{j}^n \frac{J_n'(k_{1r}R_3)}{H_n'(k_{1r}R_3)} \tag{6}$$

where $()'$ denotes the first derivative of the function with respect to the argument.

Finally, the assumed total external pressure field can be written as:

$$p_1(r,\theta,z) = A_i \sum_{n=0}^{\infty} \varepsilon_n \mathrm{j}^n \left[J_n(k_{1r}r) - \frac{J_n'(k_{1r}R_3)}{H_n'(k_{1r}R_3)} H_n(k_{1r}r) \right] \cos\left(n(\theta - \theta_i)\right) e^{\mathrm{j}k_{1z}z} \tag{7}$$

Using the Wronski determinant $J_n(r) H_n'(r) - J_n'(r) H_n(r) = \frac{2\mathrm{j}}{\pi r}$ and evaluating Eq. (7) at the cylinder surface $r = R_3$ yield to the expression of the blocked-wall pressure:

$$p_1(r,\theta,z)\big|_{r=R_3} = \frac{2\mathrm{j}A_i}{\pi k_{1r} R_3} \sum_{n=0}^{\infty} \varepsilon_n \mathrm{j}^n \frac{1}{H_n'(k_{1r}R_3)} \cos\left(n(\theta - \theta_i)\right) e^{\mathrm{j}k_{1z}z} \tag{8}$$

In this study, it must be noted that the excitation is supposed to be the blocked pressure of the cylinder as derived in Eq. (8), however the added impedance on the structure due to the external fluid is not taken into account.

3.2. Pressure field in the acoustic cavity

The fluid properties in the acoustic cavity Ω_2 are the density ρ_2 and the speed of sound c_2. The transmitted pressure p_2 in the closed cavity satisfies the Helmoltz equation and the axial boundary condition:

$$\Delta p_2 + k_2^2 p_2 = 0 \qquad \text{in } \Omega_2 \tag{9a}$$

$$\frac{1}{\rho_2 \omega^2} \nabla p_2 . \vec{e}_z = 0 \qquad \text{on } z = 0, L \tag{9b}$$

where Δ is the Laplacian operator and $k_2 = \frac{\omega}{c_2}$ the wave number in the cavity.

The pressure field p_2 satisfying Eq. (9) is given by:

$$p_2(r,\theta,z) = \sum_{n=0}^{\infty} \sum_{m=0}^{\infty} P^{nm} J_n(k_{2rm} r) \cos\left(\frac{m\pi}{L} z\right) \cos\left(n(\theta - \theta_i)\right) \tag{10}$$

where $k_{2rm} = \sqrt{\left(\frac{\omega}{c_2}\right)^2 - \left(m\frac{\pi}{L}\right)^2}$ is the radial wave number of order m and P^{nm} are the unknown magnitudes of (n,m) order.

Note that for a given mode m and angular frequency ω where $\frac{\omega}{c_2} < m\frac{\pi}{L}$, the radial wavenumber is a pure imaginary number $k_{2rm} = \mathrm{j}\sqrt{\left(m\frac{\pi}{L}\right)^2 - \left(\frac{\omega}{c_2}\right)^2}$. Using the identity between the Bessel function of first kind and order n J_n and the modified Bessel function I_n of first kind and order n for a pure imaginary argument $J_n(\mathrm{j}k_{2rm}r) = \mathrm{j}^n I_n(k_{2rm}r)$, the transmitted pressure Eq. (10) is expressed accordingly to the dispersion relation:

- For $\frac{\omega}{c_2} > m\frac{\pi}{L}$:

$$k_{2rm} = \sqrt{\left(\frac{\omega}{c_2}\right)^2 - \left(m\frac{\pi}{L}\right)^2} \tag{11a}$$

$$p_2(r,\theta,z) = \sum_{n=0}^{\infty}\sum_{m=0}^{\infty} P^{nm} J_n\left(k_{2rm} r\right)\cos\left(\frac{m\pi}{L}z\right)\cos\left(n\left(\theta-\theta_i\right)\right) \tag{11b}$$

- For $\frac{\omega}{c_2} < m\frac{\pi}{L}$:

$$k_{2rm} = \sqrt{\left(m\frac{\pi}{L}\right)^2 - \left(\frac{\omega}{c_2}\right)^2} \tag{12a}$$

$$p_2(r,\theta,z) = \sum_{n=0}^{N}\sum_{m=0}^{M} P^{nm} I_n\left(k_{2rm} r\right)\cos\left(\frac{m\pi}{L}z\right)\cos\left(n\left(\theta-\theta_i\right)\right) \tag{12b}$$

where k_{2rm} is the radial wave number satisfying the dispersion relations Eqs. (11a) and (12a). The decomposition of the cavity pressure expression has been made for numerical implementation reasons.

4. Motion of the laminated composite shell

First-order Shear Deformation Theory (FSDT) is used to describe the motion of the laminated composite cylindrical shell where the contribution of shear and rotational inertia effects are taken into account. As one can refer to Refs. [39,40], the displacement field of the skin $\boldsymbol{U}_s$ is given by:

$$\begin{bmatrix} u(r,\theta,z) \\ v(r,\theta,z) \\ w(r,\theta,z) \end{bmatrix} = \begin{bmatrix} u_0(\theta,z) + \xi\psi_z(\theta,z) \\ v_0(\theta,z) + \xi\psi_\theta(\theta,z) \\ w_0(\theta,z) \end{bmatrix} \tag{13}$$

where (u,v,w) are the displacement components in (z,θ,r) directions respectively; (u_0,v_0,w_0) are the midsurface normal line translations in (z,θ,r) directions respectively and (ψ_z,ψ_θ) are the midsurface normal line rotations in (z,r) plane and (θ,r) plane respectively; and $\xi = r - R_m$ is the height from the shell mid-surface with R_m being the shell midsurface radius.

The governing shell equations are expressed for a harmonic motion:

$$\frac{\partial N_z}{\partial z} + \frac{1}{R_m}\frac{\partial N_{\theta z}}{\partial \theta} + F_u = -\omega^2\left(\bar{I}_1 u_0 + \bar{I}_2\psi_z\right) \tag{14a}$$

$$\frac{1}{R_m}\frac{\partial N_\theta}{\partial \theta} + \frac{\partial N_{z\theta}}{\partial z} + \frac{Q_\theta}{R_m} + F_v = -\omega^2\left(\bar{I}_1 v_0 + \bar{I}_2\psi_\theta\right) \tag{14b}$$

$$\frac{\partial Q_z}{\partial z} + \frac{1}{R_m}\frac{\partial Q_\theta}{\partial \theta} - \frac{N_\theta}{R_m} + F_w = -\omega^2\bar{I}_1 w_0 \tag{14c}$$

$$\frac{\partial M_z}{\partial z} + \frac{1}{R_m}\frac{\partial M_{\theta z}}{\partial \theta} - Q_z + M_{\psi_z} = -\omega^2\left(\bar{I}_2 u_0 + \bar{I}_3\psi_z\right) \tag{14d}$$

$$\frac{1}{R_m}\frac{\partial M_\theta}{\partial \theta} + \frac{\partial M_{z\theta}}{\partial z} - Q_\theta + M_{\psi_\theta} = -\omega^2\left(\bar{I}_2 v_0 + \bar{I}_3\psi_\theta\right) \tag{14e}$$

where the generalized stresses $(N_z, N_\theta, N_{z\theta}, N_{\theta z})$ are the membrane force resultants, $(M_z, M_\theta, M_{z\theta}, M_{\theta z})$ the moment resultants, (Q_z, Q_θ) the shear force resultants, $(\bar{I}_1, \bar{I}_2, \bar{I}_3)$ the inertial coefficients and (F_u, F_v, F_w) and $\left(M_{\psi_z}, M_{\psi_\theta}\right)$ are the external resultant forces and momentum (per unit area) respectively. The first three equations in Eq. (14) describe the balance of resultant forces, while the last two equations describe the balance of momentum.

The constitutive equations relating the generalized stresses to the generalized strains and curvature changes of the middle surface are given in matrix forms:

$$\begin{bmatrix} N_z \\ N_\theta \\ N_{z\theta} \\ N_{\theta z} \\ M_z \\ M_\theta \\ M_{z\theta} \\ M_{\theta z} \end{bmatrix} = \begin{bmatrix} \bar{A}_{11} & A_{12} & 0 & 0 & \bar{B}_{11} & B_{12} & 0 & 0 \\ A_{12} & \hat{A}_{22} & 0 & 0 & B_{12} & \hat{B}_{22} & 0 & 0 \\ 0 & 0 & \bar{A}_{66} & A_{66} & 0 & 0 & \bar{B}_{66} & B_{66} \\ 0 & 0 & A_{66} & \hat{A}_{66} & 0 & 0 & B_{66} & \hat{B}_{66} \\ \bar{B}_{11} & B_{12} & 0 & 0 & \bar{D}_{11} & D_{12} & 0 & 0 \\ B_{12} & \hat{B}_{22} & 0 & 0 & D_{12} & \hat{D}_{22} & 0 & 0 \\ 0 & 0 & \bar{B}_{66} & B_{66} & 0 & 0 & \bar{D}_{66} & D_{66} \\ 0 & 0 & B_{66} & \hat{B}_{66} & 0 & 0 & D_{66} & \hat{D}_{66} \end{bmatrix} \begin{bmatrix} \varepsilon_{0z} \\ \varepsilon_{0\theta} \\ \varepsilon_{0z\theta} \\ \varepsilon_{0\theta z} \\ \kappa_z \\ \kappa_\theta \\ \kappa_{z\theta} \\ \kappa_{\theta z} \end{bmatrix} \tag{15a}$$

$$\begin{bmatrix} Q_z \\ Q_\theta \end{bmatrix} = \begin{bmatrix} \bar{A}_{55} & 0 \\ 0 & \hat{A}_{44} \end{bmatrix} \begin{bmatrix} \gamma_{0zr} \\ \gamma_{0\theta r} \end{bmatrix} \tag{15b}$$

where $(\varepsilon_{0z}, \varepsilon_{0\theta}, \varepsilon_{0z\theta}, \varepsilon_{0\theta z}, \gamma_{0zr}, \gamma_{0\theta r})$ are the midsurface strains and $(\kappa_z, \kappa_\theta, \kappa_{z\theta}, \kappa_{\theta z})$ are the curvature and twist changes formulated as:

$$\varepsilon_{0z} = \frac{\partial u_0}{\partial z} \tag{16a}$$

$$\varepsilon_{0\theta} = \frac{\partial v_0}{R_m \partial \theta} + \frac{w_0}{R_m} \tag{16b}$$

$$\varepsilon_{0z\theta} = \frac{\partial v_0}{\partial z} \tag{16c}$$

$$\varepsilon_{0\theta z} = \frac{\partial u_0}{R_m \partial \theta} \tag{16d}$$

$$\kappa_z = \frac{\partial \psi_z}{\partial z} \tag{16e}$$

$$\kappa_\theta = \frac{\partial \psi_\theta}{R_m \partial \theta} \tag{16f}$$

$$\kappa_{z\theta} = \frac{\partial \psi_\theta}{\partial z} \tag{16g}$$

$$\kappa_{\theta z} = \frac{\partial z}{R_m \partial \psi_\theta} \tag{16h}$$

$$\gamma_{0zr} = \frac{\partial w_0}{\partial z} + \psi_z \tag{16i}$$

$$\gamma_{0\theta r} = \frac{\partial w_0}{R_m \partial \theta} - \frac{v_0}{R_m} + \psi_\theta \tag{16j}$$

The shell inertial coefficients $(\bar{I}_1, \bar{I}_2, \bar{I}_3)$ as well as the shell constitutive constants Eq. (15) can be found in Appendix A in terms of shell properties.

Using Eqs. (15), (16) in Eq. (14), the governing shell equations expressed in terms of displacement variables are written in a concise matrix form:

$$\left[\boldsymbol{K}_{\mathrm{cq}}\right] \cdot \left\{\boldsymbol{U}_{cq}\right\} - \omega^2 \left[\boldsymbol{M}_{\mathrm{cq}}\right] \cdot \left\{\boldsymbol{U}_{cq}\right\} + \left\{\boldsymbol{q}_-\right\} + \left\{\boldsymbol{q}_+\right\} = 0 \tag{17}$$

where $\boldsymbol{K}_{\mathrm{cq}}$ and $\boldsymbol{M}_{\mathrm{cq}}$ denote the generalized stiffness and inertial operators respectively and $\boldsymbol{q}_-$ and $\boldsymbol{q}_+$ the generalized external forces and moments vectors applied on the inner and outer surfaces respectively. The coefficients of the stiffness operator $\boldsymbol{K}_{\mathrm{cq}}$ and the inertial operator $\boldsymbol{M}_{\mathrm{cq}}$ can be found in Ref. [39] while the expression of the external forces will be detailed in Section 6.

Considering a clamped–clamped shell to the rigid baffles, the axial boundary conditions in terms of shell midsurface displacements write:

$$u_0(\theta, z) = 0 \qquad \text{on } z = 0, L \tag{18a}$$

$$v_0(\theta, z) = 0 \qquad \text{on } z = 0, L \tag{18b}$$

$$w_0(\theta, z) = 0 \qquad \text{on } z = 0, L \tag{18c}$$

$$\psi_z(\theta, z) = 0 \qquad \text{on } z = 0, L \tag{18d}$$

$$\psi_\theta(\theta, z) = 0 \qquad \text{on } z = 0, L \tag{18e}$$

Using cylindrical harmonic decomposition for the azimuthal dependence, and Rayleigh–Ritz trigonometric expansion for the axial dependence while satisfying the boundary conditions Eq. (18), the expression of shell variables are given by:

$$u_0(\theta, z) = \sum_{n=0}^{\infty} \sum_{m=1}^{\infty} u_0^{nm} \cos\left(n\left(\theta - \theta_i\right)\right) \sin\left(\frac{m\pi}{L} z\right) \tag{19a}$$

$$v_0(\theta, z) = \sum_{n=0}^{\infty} \sum_{m=1}^{\infty} v_0^{nm} \sin\left(n\left(\theta - \theta_i\right)\right) \sin\left(\frac{m\pi}{L} z\right) \tag{19b}$$

$$w_0(\theta, z) = \sum_{n=0}^{\infty} \sum_{m=1}^{\infty} w_0^{nm} \cos\left(n\left(\theta - \theta_i\right)\right) \sin\left(\frac{m\pi}{L} z\right) \tag{19c}$$

$$\psi_z(\theta, z) = \sum_{n=0}^{\infty} \sum_{m=1}^{\infty} \psi_z^{nm} \cos\left(n\left(\theta - \theta_i\right)\right) \sin\left(\frac{m\pi}{L} z\right) \tag{19d}$$

$$\psi_\theta(\theta, z) = \sum_{n=0}^{\infty} \sum_{m=1}^{\infty} \psi_\theta^{nm} \sin\left(n\left(\theta - \theta_i\right)\right) \sin\left(\frac{m\pi}{L} z\right) \tag{19e}$$

where $(u_0^{nm}, v_0^{nm}, w_0^{nm}, \psi_z^{nm}, \psi_\theta^{nm})$ are the unknown magnitudes of (n, m) order.

Other than clamped–clamped conditions Eq. (18), the proposed model can also consider different shell boundary conditions such as simply-supported, free–free or clamped–free conditions, and hence the displacement solution should differ from the expression Eq. (19) accordingly in terms of circular functions (sine and cosine) and axial wave number.

5. Motion of the poroelastic core

The wave propagation through the poroelastic core is described with full 3D Biot's theory for homogeneous and isotropic materials [1,41]. The model considers elastic frame fully saturated with fluid phase and takes into account their different physical couplings. Using the mixed u-p formulation [42,43], the skeleton displacement vector $\boldsymbol{U}^s = \left\{U_r, U_\theta, U_z\right\}^t$ and acoustic pressure in the interstitial fluid P_f satisfy the modified Biot equations:

$$\nabla.\left(\hat{\boldsymbol{\sigma}}^s - \alpha\phi P_f \mathbf{I}\right) + \tilde{\rho}\omega^2 \boldsymbol{U}^s + \beta\nabla\left(\phi P_f\right) = 0 \tag{20a}$$

$$\nabla.\left(\frac{1}{\tilde{\rho}_{22}\omega^2}\nabla\left(\phi P_f\right) - \beta\boldsymbol{U}^s\right) + \frac{\phi P_f}{\tilde{R}} + \alpha\nabla.\boldsymbol{U}^s = 0 \tag{20b}$$

where $\mathbf{I}$ is the identity operator, ϕ the material porosity, $\hat{\boldsymbol{\sigma}}^s$ the *in vacuo* skeleton stress tensor; $\tilde{R}$ the fluid effective bulk modulus; $\tilde{\rho}$, $\tilde{\rho}_{22}$ are the effective skeleton and fluid densities respectively; and α, β the dimensionless elastic and inertial skeleton–fluid couplings respectively. In addition to elastic and inertial couplings, the adopted model includes the viscous and thermal dissipation using the Johnson–Champoux–Allard model [41,44,45]. The expression of model parameters in terms of poroelastic properties are given in Appendix B and more details can be found in Ref. [41].

The *in vacuo* skeleton stress tensor is related to the skeleton displacement with Hooke's law:

$$\hat{\boldsymbol{\sigma}}^s = \lambda\left(\nabla.\boldsymbol{U}^s\right)\boldsymbol{I} - \mu\left(\nabla\boldsymbol{U}^s + \left(\nabla\boldsymbol{U}^s\right)^t\right) \tag{21}$$

where λ and μ are the Lamé coefficients. And the interstitial fluid displacement is related to the acoustic pressure and skeleton displacement by the following formula:

$$\boldsymbol{U}^f = \frac{1}{\tilde{\rho}_{22}\omega^2}\nabla\left(\phi P_f\right) - \frac{\tilde{\rho}_{12}}{\tilde{\rho}_{22}}\boldsymbol{U}^s \tag{22}$$

Assuming the core is axially clamped–clamped to rigid baffles on its edges, the boundary condition writes:

$$\boldsymbol{U}^s = 0 \qquad \text{on} \quad z = 0, L \tag{23a}$$

$$\boldsymbol{U}^f.\vec{\boldsymbol{e}}_z = 0 \qquad \text{on} \quad z = 0, L \tag{23b}$$

The first equation Eq. (23a) refer to the nullity of the skeleton displacement vector, while the second equation Eq. (23b) describes the nullity of the normal component of the fluid displacement vector.

In the same way as previously exposed for the shell motion, using cylindrical harmonics decomposition for azimuthal dependence and Rayleigh–Ritz trigonometric expansion for axial dependence while satisfying clamped–clamped boundary condition Eq. (23), the poroelastic variables are given by:

$$U_r(r,\theta,z) = \sum_{n=0}^{\infty}\sum_{m=1}^{\infty} U_r^{nm}(r)\cos\left(n\left(\theta-\theta_i\right)\right)\sin\left(\frac{m\pi}{L}z\right) \tag{24a}$$

$$U_\theta(r,\theta,z) = \sum_{n=0}^{\infty}\sum_{m=1}^{\infty} U_\theta^{nm}(r)\sin\left(n\left(\theta-\theta_i\right)\right)\sin\left(\frac{m\pi}{L}z\right) \tag{24b}$$

$$U_z(r,\theta,z) = \sum_{n=0}^{\infty}\sum_{m=1}^{\infty} U_z^{nm}(r)\cos\left(n\left(\theta-\theta_i\right)\right)\sin\left(\frac{m\pi}{L}z\right) \tag{24c}$$

$$P_f(r,\theta,z) = \sum_{n=0}^{\infty}\sum_{m=0}^{\infty} P_f^{nm}(r)\cos\left(n\left(\theta-\theta_i\right)\right)\cos\left(\frac{m\pi}{L}z\right) \tag{24d}$$

where $\left(U_r^{nm}, U_\theta^{nm}, U_z^{nm}, P_f^{nm}\right)$ are unknown functions of order (n,m) and depending on the radius r.

At this point, the wave propagation dependence in the poroelastic material described by the variables $\left(U_r, U_\theta, U_z, P_f\right)$ is known with respect to azimuthal and longitudinal spatial coordinates θ and z, while the radial dependence r is still unknown. Since there is no *a priori* closed form to describe the wave propagation through the core thickness with Rayleigh–Ritz expansion, FEM approximation will be used instead.

For this purpose, the poroelastic thickness domain $\left[R_1, R_2\right]$ is divided into elements and the unknown functions $\left(U_r^{nm}, U_\theta^{nm}, U_z^{nm}, P_f^{nm}\right)$ are interpolated with a combination of shape functions:

$$\left[U_r^{nm}, U_\theta^{nm}, U_z^{nm}, P_f^{nm}\right](r) = \sum_{i=1}^{I}\psi_i(r)\left[U_r^{nmi}, U_\theta^{nmi}, U_z^{nmi}, P_f^{nmi}\right] \tag{25}$$

where $\left(U_r^{nmi}, U_\theta^{nmi}, U_z^{nmi}, P_f^{nmi}\right)$ are the ith nodal values of (n,m) order and ψ_i the shape function associated to the FEM expansion.

Using Eq. (25) in Eq. (24) yields to the expressions of poroelastic skeleton displacement (U_r, U_θ, U_z) and fluid pressure P_f given as follows:

$$U_r(r,\theta,z) = \sum_{n=0}^{\infty}\sum_{m=1}^{\infty}\sum_{i=1}^{I} U_r^{nmi}\psi_i(r)\cos\left(n\left(\theta-\theta_i\right)\right)\sin\left(\frac{m\pi}{L}z\right) \tag{26a}$$

$$U_\theta(r,\theta,z) = \sum_{n=0}^{\infty}\sum_{m=1}^{\infty}\sum_{i=1}^{I} U_\theta^{nmi}\psi_i(r)\sin\left(n\left(\theta-\theta_i\right)\right)\sin\left(\frac{m\pi}{L}z\right) \tag{26b}$$

$$U_z(r,\theta,z) = \sum_{n=0}^{\infty}\sum_{m=1}^{\infty}\sum_{i=1}^{I} U_z^{nmi}\psi_i(r)\cos\left(n\left(\theta-\theta_i\right)\right)\sin\left(\frac{m\pi}{L}z\right) \tag{26c}$$

$$P_f(r,\theta,z) = \sum_{n=0}^{\infty}\sum_{m=0}^{\infty}\sum_{i=1}^{I} P_f^{nmi}\psi_i(r)\cos\left(n\left(\theta-\theta_i\right)\right)\cos\left(\frac{m\pi}{L}z\right) \tag{26d}$$

where $\left(U_r^{nmi}, U_\theta^{nmi}, U_z^{nmi}, P_f^{nmi}\right)$ are the unknown magnitudes of porous media of (n,m,i) order. Note that for the skeleton displacement $\boldsymbol{U}^s$, the first longitudinal order starts from $m=1$; while for the pressure field P_f, the first longitudinal order starts from $m=0$.

6. Coupling conditions

6.1. Shell and external fluid coupling

The external generalized force vector $\boldsymbol{q}_+$ applied by the external fluid on the outer surface of the shell S_3 is given by:

$$\{\boldsymbol{q}_+\} = \left\{0, \quad 0, \quad -p_1\big|_{r=R_3}, \quad 0, \quad 0\right\}^t \tag{27}$$

6.2. Poroelastic core and shell coupling

The poroelastic core is bounded to the shell and the coupling conditions are given by:

$$U_r = w \qquad \text{on } r=R_2 \tag{28a}$$

$$U_\theta = v \qquad \text{on } r=R_2 \tag{28b}$$

$$U_z = u \qquad \text{on } r=R_2 \tag{28c}$$

$$\left(\boldsymbol{U}^s - \boldsymbol{U}^f\right).\vec{\boldsymbol{e}}_r = 0 \qquad \text{on } r=R_2 \tag{28d}$$

The first three equations of Eq. (28) expresses the solid–solid displacement continuity while the last equation expresses the nullity of the relative displacement between the skeleton and the interstitial fluid normally to the interface.

Let us denote by $\boldsymbol{T} = \left\{T_r, T_\theta, T_z\right\}^t$ the transmitted stress vector at the shell and poroelastic interface S_2. One can show that the cylindrical expansion of the transmitted stress vector $\boldsymbol{T}$ is given by:

$$T_r = \sum_{n=0}^{\infty} T_{rn}\cos\left(n\left(\theta-\theta_i\right)\right) \tag{29a}$$

$$T_\theta = \sum_{n=0}^{\infty} T_{\theta n}\sin\left(n\left(\theta-\theta_i\right)\right) \tag{29b}$$

$$T_z = \sum_{n=0}^{\infty} T_{zn}\cos\left(n\left(\theta-\theta_i\right)\right) \tag{29c}$$

Hence, the generalized forces and moments applied on the inner surface of the shell are given by:

$$\{\boldsymbol{q}_-\} = \left\{T_z, \quad T_\theta, \quad T_z, \quad -\frac{h}{2}T_z, \quad -\frac{h}{2}T_\theta\right\}^t \tag{30}$$

with $h = R_3 - R_2$ being the total shell thickness.

6.3. Acoustic cavity and poroelastic core coupling

On the interface of the acoustic cavity and the poroelastic core S_1, the continuity of the normal displacement can be written as:

$$\frac{1}{\rho_2\omega^2}\nabla p_2.\vec{\boldsymbol{e}}_r = \boldsymbol{U}^s.\vec{\boldsymbol{e}}_r + \phi\left(\boldsymbol{U}^s - \boldsymbol{U}^f\right).\vec{\boldsymbol{e}}_r \quad \text{on } r=R_1 \tag{31}$$

Reciprocally, the continuity of the stress vector is given by:

$$\left(\hat{\boldsymbol{\sigma}}^s - \alpha\phi P_f\mathbf{I}\right).\vec{\boldsymbol{e}}_r = -p_2\vec{\boldsymbol{e}}_r \quad \text{on } r=R_1 \tag{32}$$

Considering closed pores at the interface S_1 (the interstitial fluid is isolated from the cavity), the nullity of the normal relative displacement between the skeleton and interstitial fluid writes:

$$\left(\boldsymbol{U}^s - \boldsymbol{U}^f\right).\vec{\boldsymbol{e}}_r = 0 \quad \text{on } r = R_1 \tag{33}$$

Using Eq. (33), the acoustic cavity and poroelastic core coupling condition Eq. (31) is simplified into:

$$\frac{1}{\rho_2\omega^2}\nabla p_2.\vec{\boldsymbol{e}}_r = \boldsymbol{U}^s.\vec{\boldsymbol{e}}_r \quad \text{on } r = R_1 \tag{34}$$

7. Assembled global vibro-acoustic problem

In order to assemble the vibro-acoustic problem, one has to derive the weak formulation of the governing equations and boundary conditions based on Galerkin method:

1. In the acoustic cavity:

$$\int_{\Omega_1}\left[\frac{1}{\rho_2\omega^2}\nabla\left(\delta p_2\right).\nabla\left(p_2\right) - \frac{1}{\rho_2 c_2^2}\delta p_2.p_2\right]d\upsilon - \int_{S_1}\delta p_2.\left[\boldsymbol{U}^s.\vec{\boldsymbol{e}}_r + \underbrace{\phi\left(\boldsymbol{U}^s - \boldsymbol{U}^f\right).\vec{\boldsymbol{e}}_r}_{0}\right]ds = 0 \tag{35a}$$

2. In the poroelastic domain:

$$\int_{\Omega_p}\left[\boldsymbol{\varepsilon}\left(\delta\boldsymbol{U}^s\right)^t : \boldsymbol{K}_{\text{pe}} : \boldsymbol{\varepsilon}\left(\boldsymbol{U}^s\right) - \omega^2\tilde{\rho}\,\delta\boldsymbol{U}^s.\boldsymbol{U}^s\right]d\upsilon + \int_{\Omega_p}\left[\alpha\phi\,\nabla\left(\delta.\boldsymbol{U}^s\right).P_f + \beta\phi\,\delta\boldsymbol{U}^s.\nabla\left(P_f\right)\right]d\upsilon$$
$$- \int_{S_1}\left(\delta\boldsymbol{U}^s.\vec{\boldsymbol{e}}_r\right).p_2\,ds - \int_{S_2}\delta\boldsymbol{U}_{cq}.\boldsymbol{T}\,ds = 0 \tag{35b}$$

$$\int_{\Omega_p}\left[\frac{\phi^2}{\omega^2\tilde{\rho}_{22}}\nabla\left(\delta P_f\right).\nabla\left(P_f\right) - \frac{\phi^2}{\tilde{R}}\delta P_f.P_f\right]d\upsilon - \int_{\Omega_p}\left[\alpha\phi\,\delta P_f\nabla.\left(\boldsymbol{U}^s\right) + \beta\phi\,\nabla\left(\delta P_f\right).\boldsymbol{U}^s\right]d\upsilon = 0 \tag{35c}$$

3. At shell midsurface:

$$\int_{S_m}\delta\boldsymbol{U}_{cq}.\left[\boldsymbol{K}_{\text{cq}} - \omega^2\boldsymbol{M}_{\text{cq}}\right].\boldsymbol{U}_{cq}\,ds + \int_{S_2}\delta\boldsymbol{U}_{cq}.\boldsymbol{T}\,ds = -\int_{S_3}\delta w_0.p_1\,ds \tag{35d}$$

4. At the interface between the shell and poroelastic domain:

$$\int_{S_2}\delta\boldsymbol{T}.\left(\boldsymbol{U}_s - \boldsymbol{U}^s\right)ds = 0 \tag{35e}$$

where the test functions are spotted with δ symbol and $\boldsymbol{K}_{\text{pe}}$ is the Hooke operator of the poroelastic skeleton. The main advantages of the mixed u-p formulation are the use of a reduced number of variables compared to the u-U formulation and the use of natural and symmetric coupling conditions at the poroelastic boundaries.

Note that, since the θ and z dependencies are explicitly written in terms of circular functions and the radial dependence is known as well (Bessel functions for acoustic cavity and using polynomial interpolation for 1D-FEM in the poroelastic core thickness), all the volume and surface integrals can be evaluated analytically. Moreover, one should notice that the functions set $\{\cos(n\theta),\,\sin(n\theta)\,/n \in \mathbb{N}\}$ are orthogonal along the cylinder circumference $\left[\theta_i, \theta_i + 2\pi\right]$ which describes a full period (or a multiple of a period). However, the functions $\left\{\cos\left(m\frac{\pi}{L}z\right),\,\sin\left(m\frac{\pi}{L}z\right)/m \in \mathbb{N}\right\}$ are not orthogonal along the cylinder length $[0, L]$ since it describes a multiple of half wavelength. Therefore, the system Eq. (37) is written for each circumferential order n separately, and the state variables are solved for all longitudinal orders $m = 0, \ldots, M$ "*at the same time*" since they are coupled. The longitudinal coupling terms are given by:

$$\int_0^L \cos\left(m_1\frac{\pi}{L}z\right)\cos\left(m_2\frac{\pi}{L}z\right)dz = \delta_{m_1m_2}\left(1 + \delta_{0m_1}\right)\frac{L}{2} \tag{36a}$$

$$\int_0^L \sin\left(m_1\frac{\pi}{L}z\right)\sin\left(m_2\frac{\pi}{L}z\right)dz = \delta_{m_1m_2}\left(1 - \delta_{0m_1}\right)\frac{L}{2} \tag{36b}$$

$$\int_0^L \sin\left(m_1\frac{\pi}{L}z\right)\cos\left(m_2\frac{\pi}{L}z\right)dz = \begin{cases} 0 & \text{if } m_1 = m_2 \\ \frac{L}{\pi}\frac{m_1}{m_1^2 - m_2^2}\left[1 - (-1)^{m_1+m_2}\right] & \text{if } m_1 \neq m_2 \end{cases} \tag{36c}$$

where $\delta_{m_1m_2} = \begin{cases} 1 & \text{if } m_1 = m_2 \\ 0 & \text{if } m_1 \neq m_2 \end{cases}$ is the Kronecker symbol. The last expression can also be written in terms of whether the sum $m_1 + m_2$ is an odd or even number.

Finally, the global vibro-acoustic problem can be written and arranged in the following matrix form:

$$\begin{bmatrix} \boldsymbol{Z}_{cq} & 0 & 0 & \boldsymbol{C}_{cq}^t \\ 0 & \boldsymbol{Z}_p & -\boldsymbol{C}_a^t & -\boldsymbol{C}_p^t \\ 0 & -\boldsymbol{C}_a & \boldsymbol{A}_a & 0 \\ \boldsymbol{C}_{cq} & -\boldsymbol{C}_p & 0 & 0 \end{bmatrix}.\begin{Bmatrix} \boldsymbol{U}_{cq} \\ \boldsymbol{U}_p \\ \boldsymbol{P}_2 \\ \boldsymbol{T} \end{Bmatrix} = \begin{Bmatrix} \boldsymbol{F}_{ex} \\ 0 \\ 0 \\ 0 \end{Bmatrix} \tag{37}$$

where $\boldsymbol{U}_{cq}, \boldsymbol{U}_p$ and $\boldsymbol{P}_2$ denote now the vectors of degrees of freedom associated to the shell, the poroelastic medium and the acoustic cavity respectively, $\boldsymbol{Z}_{cq}$ and $\boldsymbol{Z}_p$ denote shell dynamic stiffness (or impedance) and poroelastic mixed dynamic stiffness respectively, $\boldsymbol{A}_a$ acoustic cavity receptance (or admittance), $\boldsymbol{T}$ the Lagrange multiplier vector accounting for transmitted forces between shell and poroelastic material, $\boldsymbol{F}_{ex}$ the excitation pressure and $\boldsymbol{C}_{cq}, \boldsymbol{C}_p, \boldsymbol{C}_a$ the couplings operators; according to the variational expression Eq. (35).

A special attention should be carried while assembling the poroelastic operator $\boldsymbol{Z}_p$ since there is a combination of three different types of couplings between the degrees of freedom : (1) physical coupling which is given by the governing Biot equations Eq. (20) and constitutive law Eq. (21), (2) FEM couplings for nodes belonging to the same elements and (3) Rayleigh–Ritz coupling expressed in the equation Eq. (36) here above. This yields to assemble non-classical hybrid matrices which combines Rayleigh–Ritz and FEM expansions.

8. Noise reduction

In the internal acoustic cavity Ω_2, the transmitted pressure p_2 consists on standing-waves. Hence, for an enclosed acoustic cavity where the internal resonances play a major role, the sound insulation is evaluated through the Noise Reduction factor (NR). As proposed by Lesueur [33], the adopted NR expression is given by:

$$\mathrm{NR}\left(f,\phi_i\right) = 10\log_{10}\left(\frac{\left\langle p_1^2\right\rangle_S}{\left\langle p_2^2\right\rangle_V}\right) \tag{38}$$

where $f = \frac{\omega}{2\pi}$ is the frequency and $\left\langle p_1^2\right\rangle_S$ and $\left\langle p_2^2\right\rangle_V$ denote respectively the external time-surface-averaged and internal time-volume-averaged mean-square pressures given by:

$$\left\langle p_1^2\right\rangle_S = \frac{1}{T}\frac{1}{S_3}\int_0^T\int_{S_3} p_1 . p_1^* \, ds\, dt \tag{39a}$$

$$\left\langle p_2^2\right\rangle_V = \frac{1}{T}\frac{1}{\Omega_1}\int_0^T\int_{\Omega_1} p_2 . p_2^* \, dv\, dt \tag{39b}$$

with $(.)^*$ being the complex conjugate operator and the time-period $T = \frac{2\pi}{\omega}$.

Using the expressions of blocked pressure Eq. (8) and transmitted pressure Eqs. (11), (12), one can show that the averaged mean-square pressures yield to the following expressions:

$$\left\langle p_1^2\right\rangle_S = \left(\frac{2A_i}{\pi k_{1r} R_3}\right)^2 \sum_{n=0}^{\infty} \varepsilon_n \left|\frac{1}{H_n'\left(k_{1r}R_3\right)}\right|^2 \tag{40a}$$

$$\left\langle p_2^2\right\rangle_V = \frac{1}{4}\sum_{n=0}^{N}\sum_{m=0}^{M} |P^{nm}|^2 \left(1+\delta_{0n}\right)\left(1+\delta_{0m}\right) \mathrm{I}_{R_1} \tag{40b}$$

where the I_{R_1} coefficient is given by:

$$\mathrm{I}_{R_1} = \begin{cases} J_n^2\left(k_{2rm}R_1\right) - J_{n-1}\left(k_{2rm}R_1\right) J_{n+1}\left(k_{2rm}R_1\right) & \text{if } \frac{\omega}{c_2} > m\frac{\pi}{L} \\ I_n^2\left(k_{2rm}R_1\right) - I_{n-1}\left(k_{2rm}R_1\right) I_{n+1}\left(k_{2rm}R_1\right) & \text{if } \frac{\omega}{c_2} < m\frac{\pi}{L} \end{cases} \tag{41}$$

We note here that the noise reduction factor Eq. (38) depends on the excitation frequency f and on the angle of incidence ϕ_i, however it is independent from the azimuthal incidence angle θ_i which can be well understood when considering the axisymmetric property of the problem.

9. Numerical results

9.1. Computational parameters

In the present model, the unknowns are expanded into three types of expansions : harmonic expansion for the azimuthal coordinates (θ) in all media, Rayleigh–Ritz trigonometric expansion for the longitudinal coordinates (z), and Finite Element Method expansion for the radial coordinates (r) in the poroelastic core thickness. For the FEM expansion, a quadratic Lagrange polynomial interpolation is used for the poroelastic variables $\left(U_r^{nm}(r), U_\theta^{nm}(r), U_z^{nm}(r), P_f^{nm}(r)\right)$ for each (n,m) order.

In order to compute noise transmission, a sufficient expansion orders of cylindrical harmonics N and Rayleigh–Ritz approximation M have to be determined. *A priori* criterion based on *in vacuo* eigen frequencies of the structure and *rigid wall* eigen frequencies of the acoustic cavity can be formulated. The maximum orders (N, M) are determined in such a way that all resonant eigen modes in the studied frequency range are included. Henceforth solving the *in vacuo* shell eigen problem and the *rigid wall* acoustic eigen problem is the first step before solving the vibro-acoustic problem of sound transmission. Usually, for large cylinders (which is the case for aircraft or payload fairings of space launchers), the maximum orders (N, M) are fully determined by the structural eigen frequencies and not by the acoustical eigen frequencies. Furthermore, since the eigenvalue problem has already been solved, a modal projection for shell displacement $\boldsymbol{U}_{cq}$ can be exploited to improve computational time costs. This projection reduces the size of the shell related matrices $\boldsymbol{Z}_{cq}, \boldsymbol{C}_{cq}$ and the excitation vector $\boldsymbol{F}_{ex}$ while diagonalizing the dynamic stiffness operator $\boldsymbol{Z}_{cq}$.

Table 1
Naked isotropic cylinders properties (based on [33]).

Properties		Small shell	Large shell
Mid-plane radius R_m	[m]	0.221	2.162
Length L	[m]	1.026	5.715
Shell thickness	[mm]	2	2
Shell Mass density ρ	[kg/m^3]	7 800	2 768
Shell Young modulus $E_z = E_\theta$	[GPa]	200	69
Shell Poisson ratio $\nu_{z\theta} = \nu_{\theta z}$		0.3	0.3
Shell damping ratio η	[%]	5	5
Fluid Mass densities $\rho_1 = \rho_2$	[kg/m^3]	1.293	1.284
Fluid speeds of sound $c_1 = c_2$	[m/s]	340	340

In a research phase, expansions orders (N, M) could be overestimated; nonetheless a compromise between accuracy and computational cost should be found. Some adaptive schemes, as the one proposed in [20], could be useful in finding the optimal discretization parameters.

9.2. Sound transmission through naked cylinders

9.2.1. Comparison with full numerical model: small shell

The first example consists of a small isotropic cylinder made of steel and whose properties are presented in Table 1. The structural damping model is considered and the shell damping ratio η is introduced through complex elastic moduli such that:

$$\tilde{E}_\alpha = E_\alpha(1 - \mathrm{j}\,\eta) \qquad \alpha = \theta, z \tag{42a}$$

$$\tilde{G}_{\alpha\beta} = G_{\alpha\beta}(1 - \mathrm{j}\,\eta) \qquad \alpha\beta = z\theta, zr, \theta r \tag{42b}$$

The results are compared to those obtained by full numerical FEM–BEM computation using Rayon Solver [42].[1] Some discrepancies between the two models should be mentioned first : contrary to the proposed semi-analytical model, in the numerical model the rigid baffle has a sufficiently but finite length and the impedance added by the external fluid is taken into account. Moreover, and exclusively for this example, the Noise Reduction index is evaluated using the following formula:

$$\tilde{\mathrm{NR}} = -10\log_{10}\left(\left\langle p_2^2 \right\rangle_V\right) \tag{43}$$

Fig. 3 shows the sound level for an incidence angle $\phi_i = 45^o$ in the frequency range $[1, 400]$ Hz. Despite the little differences previously mentioned between the proposed semi-analytical model and full numerical FEM–BEM model, both results are in an excellent agreement. This demonstrates the validity of the assumption that the shell sound radiation in the external fluid domain is negligible in the case of a stiff cylinder coupled with a lightweight fluid. According to Fig. 3, Noise Reduction dips occur at the structural and acoustical eigen frequencies where the structural dynamic stiffness operator and acoustical receptance operator are singular respectively. It should be mentioned here that the computational effort required for the proposed semi-analytical methodology is smaller when compared to full FEM–BEM approaches. Moreover, the model does not require any FEM-type meshing of the shell and the cavity nor a BEM-type meshing of the surrounding fluid domain. This overcomes some compatibility issues sometimes encountered at the FEM–BEM coupling interface.

9.2.2. Comparison with semi-analytical model : large shell

The second example consists of an isotropic cylinder with large dimensions made of aluminum and whose properties are presented in Table 1. For large cylinder, structural and acoustical modal densities are higher and hence it requires higher discretization parameters (N, M). The NR results as defined in Eq. (38) are compared to those of Lesueur [33]. Lesueur's STL model used the Donnel-Mushtari theory to describe the shell motion and the added external impedance is included using the closed form expression of an infinitely long cylinder but integrated over the length L. Moreover, boundary conditions consist of a simply supported shell. For this purpose, the proposed model was adapted to take into account this boundary condition.

Fig. 4, Fig. 5, Fig. 6 show Noise Reduction comparisons for incidence angles $\phi_i = [90°, 45°, 15°]$ respectively. NR curves are highly fluctuating and these sharp dips represent the effects of both structural and cavity resonances. Describing the NR curves in average terms, for normal incidence $\phi_i = 90°$ the sound level inside the cavity increases with respect to the frequency. However for oblique incidence $\phi_i = 45°$, three different frequency ranges can be distinguished : in the $[1, 150]$ Hz frequency range, the NR index exhibits a decreasing tendency; in the $[150, 385]$ Hz frequency range, the NR tendency seems to be constant; above the ring frequency $f_a = 385$ Hz, the NR tends to increase. It is useful to remind here that the ring frequency corresponds to the frequency of the first breathing mode of vibration of the shell $(n = 0)$ and it occurs when the longitudinal wavelength is equal to the shell circumference [26]. The ring frequency f_a separates the stiffness controlled region $f < f_a$ from the mass controlled region $f > f_a$

[1] Rayon Solver was early developed by STRACO company and now is developed and distributed by ESI-Group in the VA-One software.

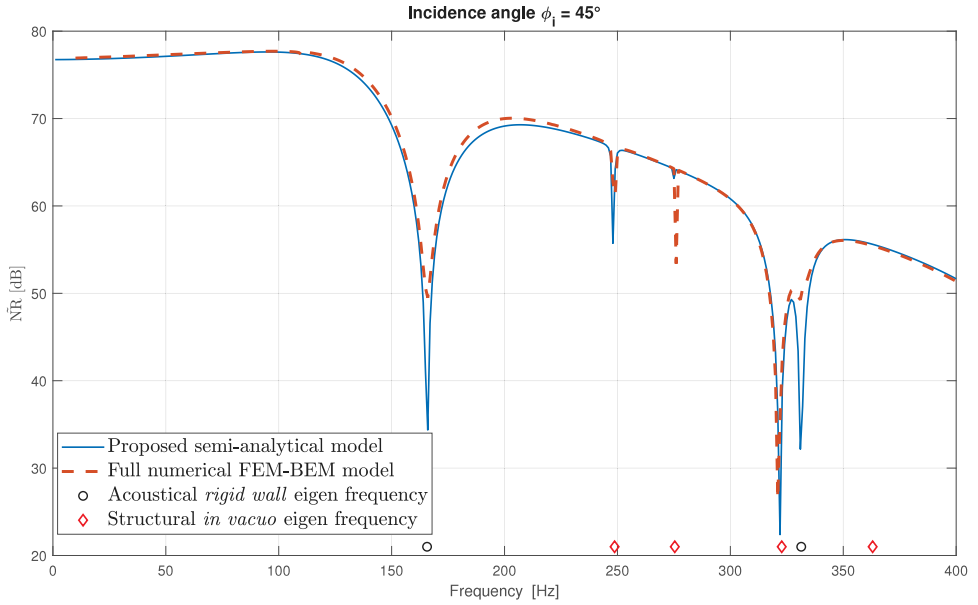

Fig. 3. Comparison of Noise Reduction $\hat{N}R$ for a small dimensions shell impinged by a plane wave with incidence angle $\phi_i = 45°$.

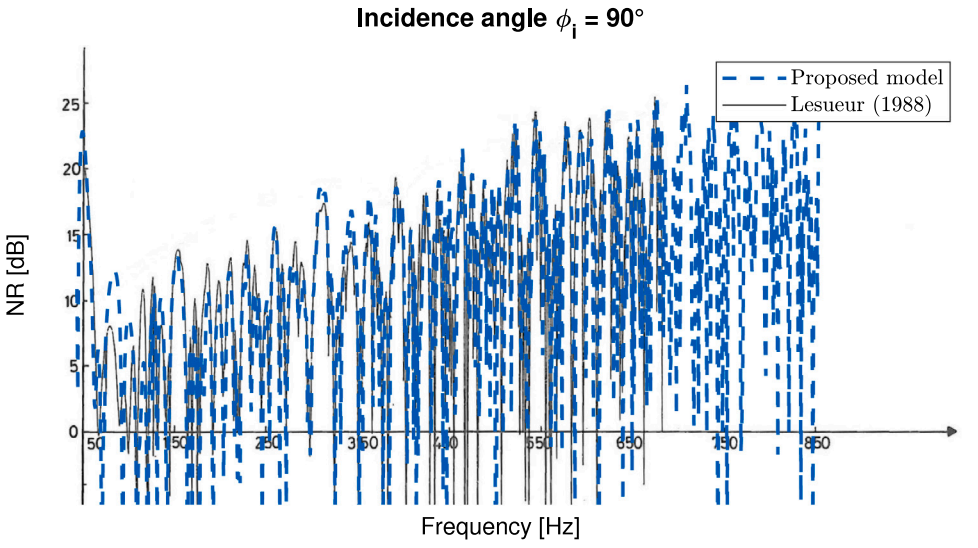

Fig. 4. Comparison of Noise Reduction for Shell A impinged by a plane wave with incidence angle $\phi_i = 90°$ (Based on [33]).

where the STL is increasing. Moreover, and according to Ref. [46] the ring frequency can be seen as the threshold of the "*resonance controlled region*" which is a transition region between the stiffness controlled region and the mass controlled region. The ring frequency expression for an orthotropic infinite shell is given by Blaise et al. [47]: $f_a = \frac{1}{2\pi R_m}\sqrt{\frac{E_\theta \zeta}{\rho\left(\zeta - \nu_{\theta z}^2\right)}}$ where $\zeta = \frac{E_\theta}{E_z}$ is the orthotropic ratio. Note that for $\zeta = 1$, the ring frequency expression for isotropic shell is found.

For oblique incidence $\phi_i = 15°$, same pattern happens and the three different frequency regions can be distinguished. However, the first frequency range is *extended* and covers $[1, 320]$ Hz while the second range is *limited* to $[320, 385]$ Hz. Above the ring frequency f_a, the NR factor increases in the mass controlled region. The proposed semi-analytical model is in a good agreement with Lesueur's results. This is in accordance with the very close structural responses given by Donnel-Mushtari shell theory and FSDT for thin isotropic cylindrical shells with a ratio $\frac{h}{R_m} \approx \frac{1}{1000}$. As it was described in the early works of Smith [48] and White [26], the minimum of noise reduction under oblique incidence is obtained at the ring frequency.

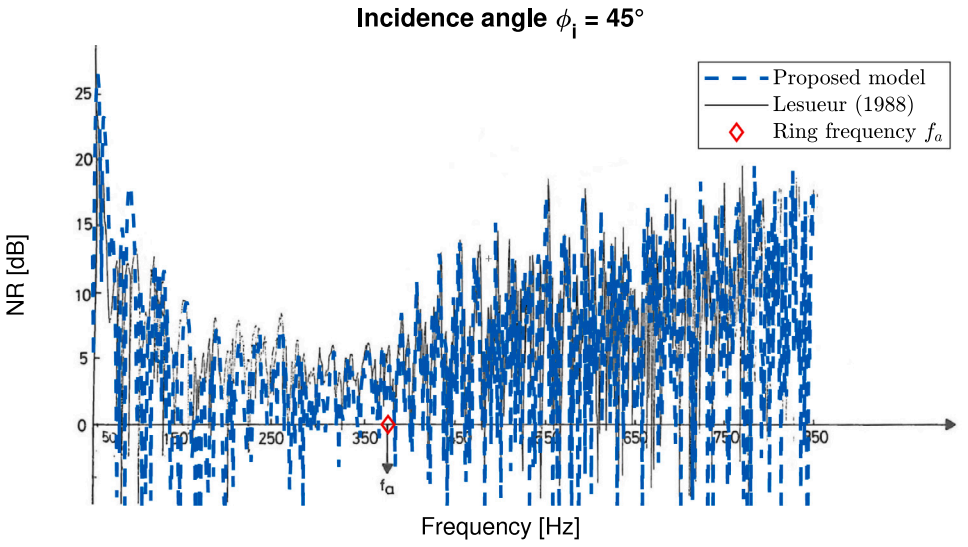

Fig. 5. Comparison of Noise Reduction for Shell A impinged by a plane wave with incidence angle $\phi_i = 45°$ (Based on [33]).

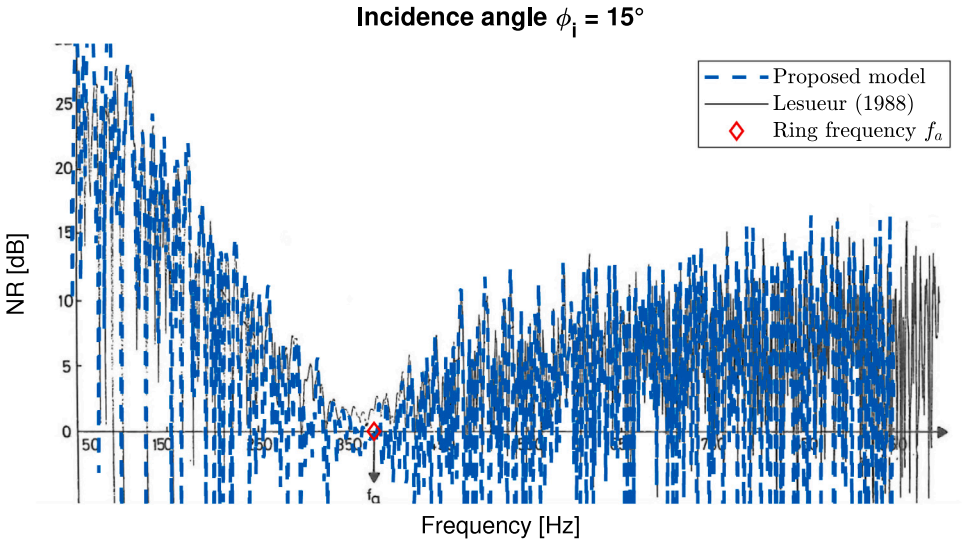

Fig. 6. Comparison of Noise Reduction for Shell A impinged by a plane wave with incidence angle $\phi_i = 15°$ (Based on [33]).

9.2.3. Finite/infinite superposition : large shell

Results obtained previously for the large isotropic cylinder case (Table. 1) are now illustrated along with those obtained by the infinitely long cylinder model established by Magniez et al. [13,15]. In these last references, the shell motion is modeled with FSDT and, unlike the presented model, the pressure radiated by the elastic cylinder in the external fluid is included. Noise Reduction juxtaposition for plane wave incidence angles $\phi_i = [90°, 45°, 15°]$ are shown in Fig. 7, Fig. 8 and Fig. 9 respectively. Results show that the finite and infinite cylinders responses present globally the same NR trends in the studied frequency range. However, huge discrepancies are observed between the two models at very low frequencies where the incident wavelengths are the largest. This is due to the effects of boundary conditions which constrain the finite shell and hence it increases its apparent stiffness. These end effects have also been observed in Refs. [19,37,38] for finite cylindrical structures as well as in Refs. [49,50] for finite flat panel structures. Despite these boundary condition effects at very low frequencies, the finite and infinite cylinders NR curves are in a good agreement globally. This is specially shown for normal incidence in Fig. 7 where both NR fluctuations match well. This NR overlapping can be partially explained by the fact that at $\phi_i = 90°$, the incident pressure p_1 is z-constant and it impinges the cylinder uniformly. For oblique incidence $\phi_i = 45°$, the infinite cylinder shows higher NR levels relatively to the finite cylinder and

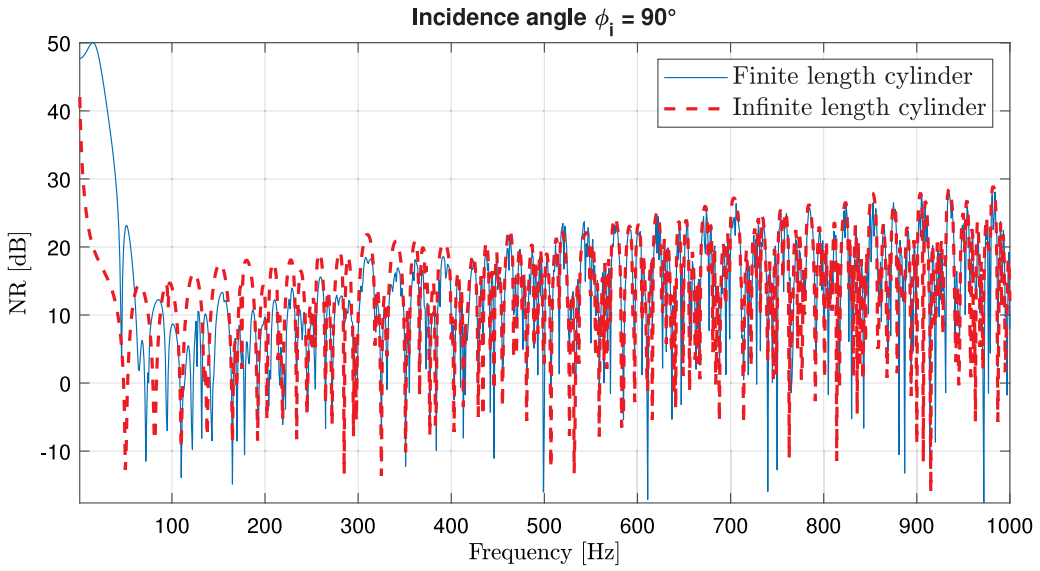

Fig. 7. Noise reduction superposition of finite length cylinder (proposed model) and infinite length cylinder (Ref. [13]) for a normal plane wave with incidence angle $\phi_i = 90^\circ$.

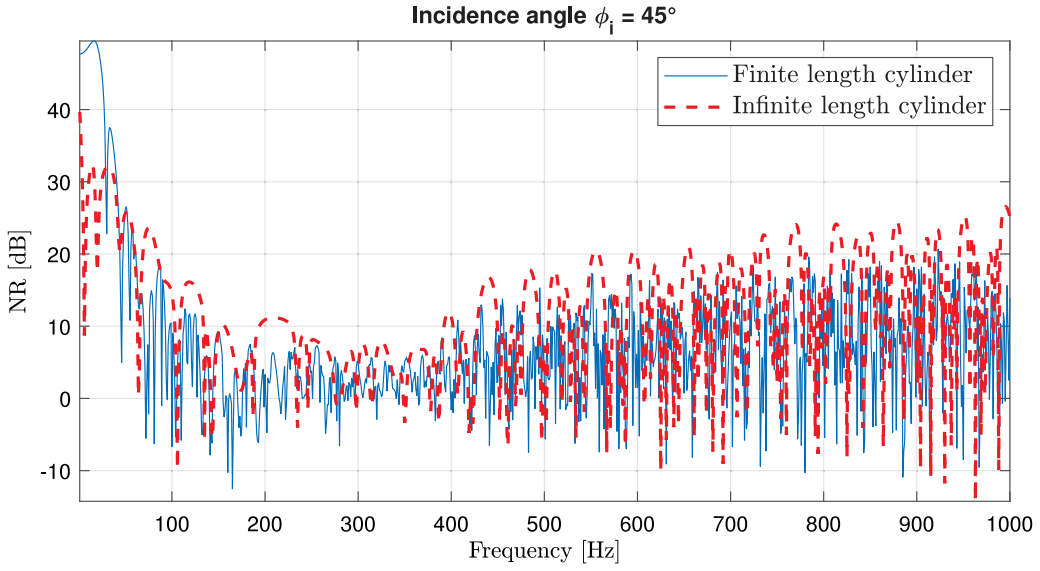

Fig. 8. Noise reduction superposition of finite length cylinder (proposed model) and infinite length cylinder (Ref. [13]) for a plane wave with incidence angle $\phi_i = 45^\circ$.

this leads to somehow overestimating the sound insulation. For small incidence angle $\phi_i = 15°$, the contrast between the finite and infinite cylinders responses is more visible where the NR index for the finite cylinder is still highly fluctuating while the NR index for infinite cylinder describes a more regular curve with fewer dips (see Fig. 9). It is also observed that the number of these dips decreases along with the decrease of angle of incidence ϕ_i. The effects of the angle of incidence on sound insulation can be explained through the examination of the acoustic waves in the internal cavity. For the finite cylinder, the transmitted pressure consists always on stationary waves in the radial and axial directions, while for the infinite cylinder the transmitted pressure consists on standing waves in the radial direction and traveling waves in the axial direction. The radial and longitudinal wave resonances involved in the finite cylinder make the NR highly fluctuating all over the frequency region regardless of the incidence angle and this tends to lower the global NR level. Besides, the radial standing waves involved in the infinite cylinder are more excited by normal incident wave than by oblique waves. This explains why the NR is more oscillating at $\phi_i = 90°$ compared to $\phi_i = 45°$ and 15°.

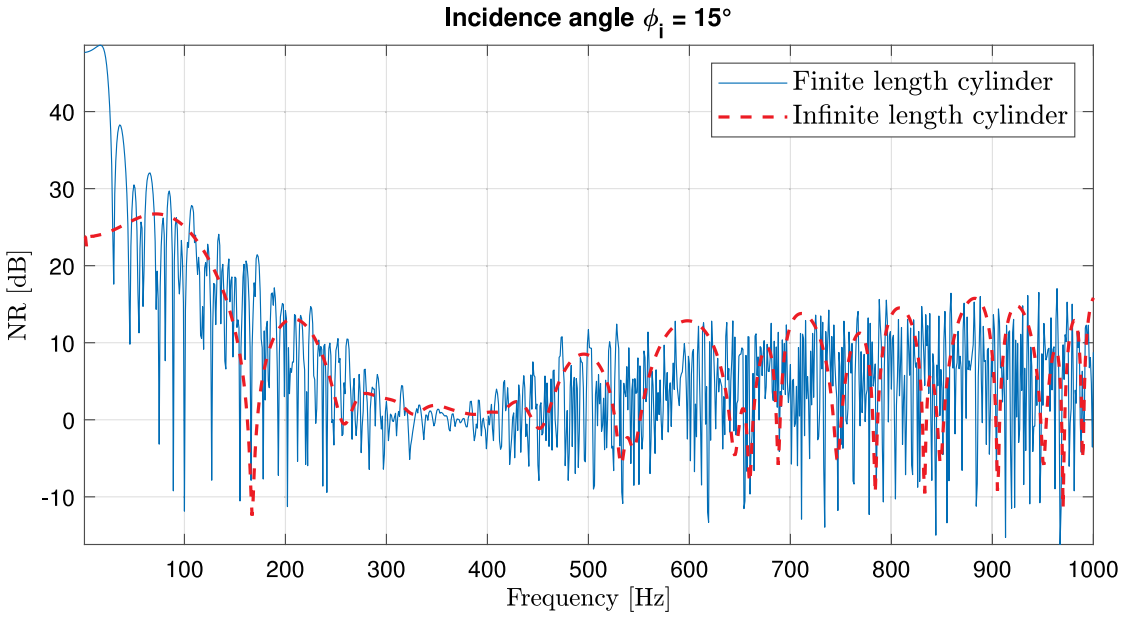

Fig. 9. Noise reduction superposition of finite length cylinder (proposed model) and infinite length cylinder (Ref. [13]) for a plane wave with incidence angle $\phi_i = 15^\circ$.

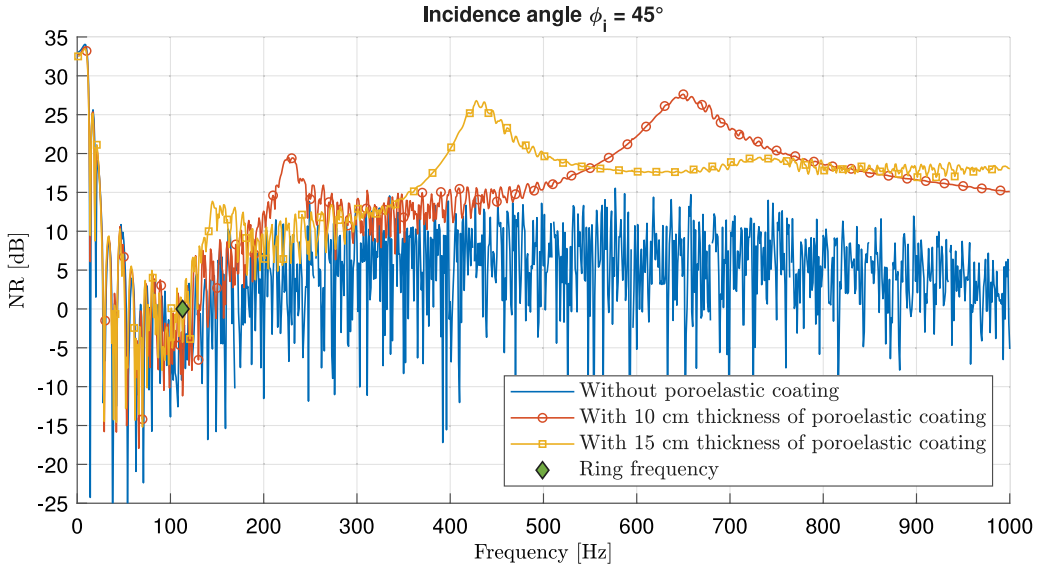

Fig. 10. Noise reduction comparison between finite length naked cylinder and finite length cylinder lined with poroelastic coating excited by a plane wave with incidence $\phi_i = 45^\circ$.

9.3. Sound transmission through laminated shell lined with poroelastic coating

In this section, the studied example consists of (an aerospace structure comprising) a cylinder of length $L = 12$ m and exterior radius $R_3 = 2.71$ m composed by a sandwich shell lined with a poroelastic coating. Two poroelastic coating thicknesses are studied : 10 cm and 15 cm thicknesses. The properties of the surrounding fluids are $\rho_1 = \rho_2 = 1.284$ kg/m^3 and $c_1 = c_2 = 340$ m/s. Shell properties, poroelastic material and interstitial fluid properties are given in Table 2 and Table 3 respectively. The poroelastic skeleton damping ratio η_s is introduced through complex elastic moduli such that:

$$\tilde{\lambda} = \lambda(1 - \mathrm{j}\,\eta_s) \tag{44a}$$

$$\tilde{\mu} = \mu(1 - \mathrm{j}\,\eta_s) \tag{44b}$$

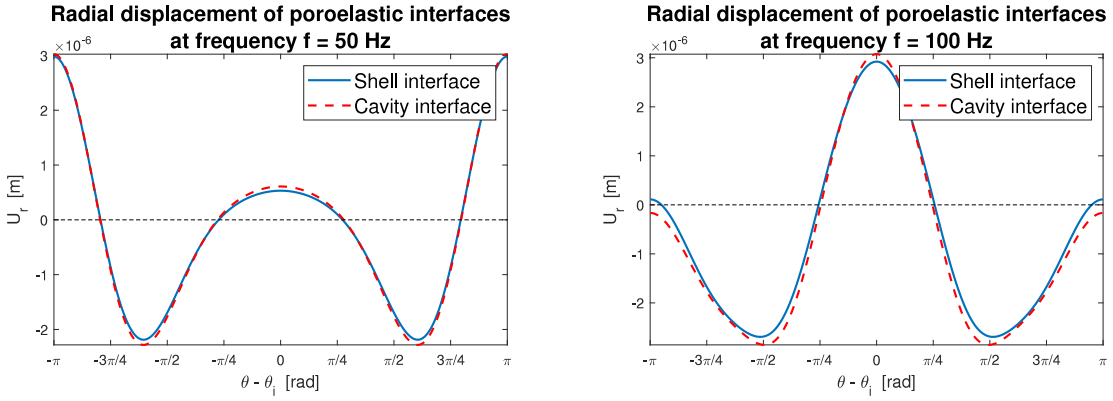

(a)

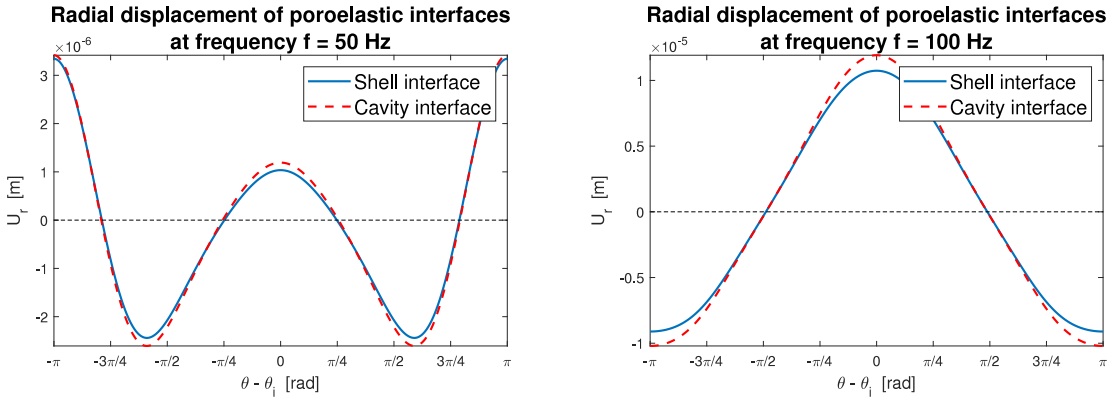

(b)

Fig. 11. Radial displacement of poroelastic coating at cross-section $z = \frac{L}{2}$ in the stiffness controlled region for a cylinder excited by a plane wave with incidence $\phi_i = 45^{\circ}$. (a) Shell lined with 10 cm thickness of poroelastic coating (b) Shell lined with 15 cm thickness of poroelastic coating.

Fig. 10 shows Noise Reduction index for naked and coated finite shell under plane wave excitation with angle of incidence $\phi_i = 45°$. The NR index is decreasing with respect to frequency reaching its minimum around the ring frequency $f_a \approx 113$ Hz and increasing above it. Below the ring frequency, no significant difference in NR level is observed between naked and coated cylinders regardless of coating thickness. In fact as stated earlier, this region corresponds to the stiffness controlled region and due to the high flexibility of the poroelastic core, the noise insulation level is not improved. In this low frequency region dominated by the stiffness of the shell, the poroelastic core follows the shell displacement with almost no radial deformation and hence no significant additional amount of acoustic energy dissipation is observed compared to naked cylinder. This is illustrated in Fig. 11 where it is observed that the radial displacement of the upper and lower interfaces of the poroelastic core are almost coincident. The upper interface corresponds to the interface with the shell and the lower interface corresponds the one with the acoustic cavity.

Just above the ring frequency, the NR level tends to increase rapidly for the three configurations and the effect of the poroelastic coating is clearly demonstrated in Fig. 10 at higher frequencies wherein the wavelengths are short enough to interact with the liner. While remaining globally constant for naked shell in the major frequency region right after the first increase, the NR factors of coated shells continue to increase and experience two rises at two different frequency locations. This point will be discussed later. Moreover, it should be noticed that the effects of internal resonances are muffled by the presence of the poroelastic coating and this is illustrated by the absence of sharp dips and less fluctuations in the NR curves. Above the ring frequency, the noise insulation is improved by the porous liner and as shown in Fig. 12 there are relative radial displacements between the poroelastic upper and lower interfaces. These relative radial vibrations cause acoustic energy dissipation and result in a higher NR level compared to naked cylinders. As pointed out earlier, NR level exhibits two peaks at around 230 Hz and 650 Hz for 10 cm coating thickness, while for 15 cm coating thickness these peaks are shifted around 150 Hz and 430 Hz respectively. The effect of a more massive coating shifts these peaks to lower frequencies. The first local NR maxima are due to skeleton resonances, and the second NR maxima are due to the classical quarter wavelength effects. These peaks can also be observed for planar structures and it is concluded that these peaks in the NR level are pure effects of the poroelastic layer resonances.

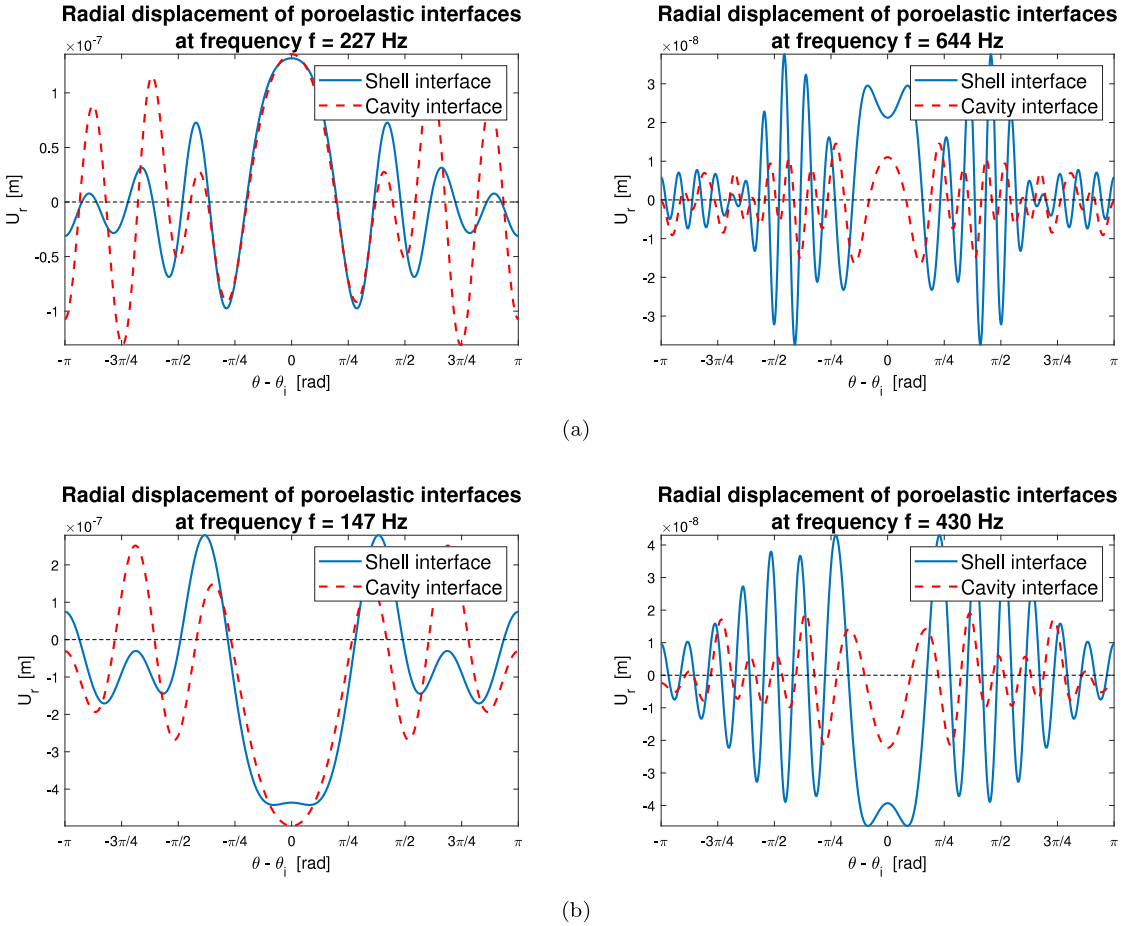

Fig. 12. Radial displacement of poroelastic coating at cross-section $z = \frac{L}{2}$ in the mass controlled region for a cylinder excited by a plane wave with incidence $\phi_i = 45^\circ$. (a) Sandwich shell lined with 10 cm thickness of poroelastic coating (b) Sandwich shell lined with 15 cm thickness of poroelastic coating.

Fig. 13, Fig. 14 and Fig. 15 show Noise Reduction superposition for coated finite and infinite length cylinder excited by a plane wave with incidence angle $\phi_i = [90°, 45°, 15°]$ respectively. For normal incidence, NR index is increasing in the frequency range and both models give very close results except at very low frequencies where the effect of boundary condition are significant. For oblique angles of incidence $\phi_i = 45°$ and 15°, just below the ring frequency, the infinite model is overestimating the NR level compared to the present finite model. Beyond the ring frequency, the discrepancies in the NR level are reduced and both models are in a good agreement. However for highly oblique incidence $\phi_i = 15°$, the NR levels are close until 600 Hz where a gap between the two models is initiated. The infinite length cylinder model shows a Noise Reduction level increase starting from around 700 Hz while the finite length cylinder model shows a Noise Reduction level increase starting from around 800 Hz for the two core thicknesses. This lag was also observed for the case of naked shell, but it is not shown here. It is concluded that the gap observed for naked shell could not be recovered with the presence of the porous liner. Moreover, the NR fluctuations intensity is higher in the stiffness controlled region rather than the mass controlled region and despite the muffling effect of the porous liner the finite internal resonances are still quite noticeable in the whole frequency region for incidence angle $\phi_i = 15°$ rather than $\phi_i = 45°$.

10. Summary and conclusion

A consistent semi-analytical model is developed to compute sound transmission through finite length multilayered cylinders impinged by incident plane waves. The cylinder is made of a laminated shell modeled with first order shear deformation theory and lined with a poroelastic core modeled by full 3D Biot's theory using u-p format. The solution is expanded into cylindrical harmonics for the azimuthal direction and, while obtaining analytical expressions of the sound pressures in the fluid domains, Rayleigh–Ritz trigonometric approximation is used to ensure the axial boundary condition of the structure. Furthermore, a quadratic finite element approximation is used to describe the radial wave propagation through the poroelastic core thickness. A weak formulation is hence derived and evaluated analytically to solve the coupled vibro-acoustic problem and an analytical expression of the Noise Reduction index is established.

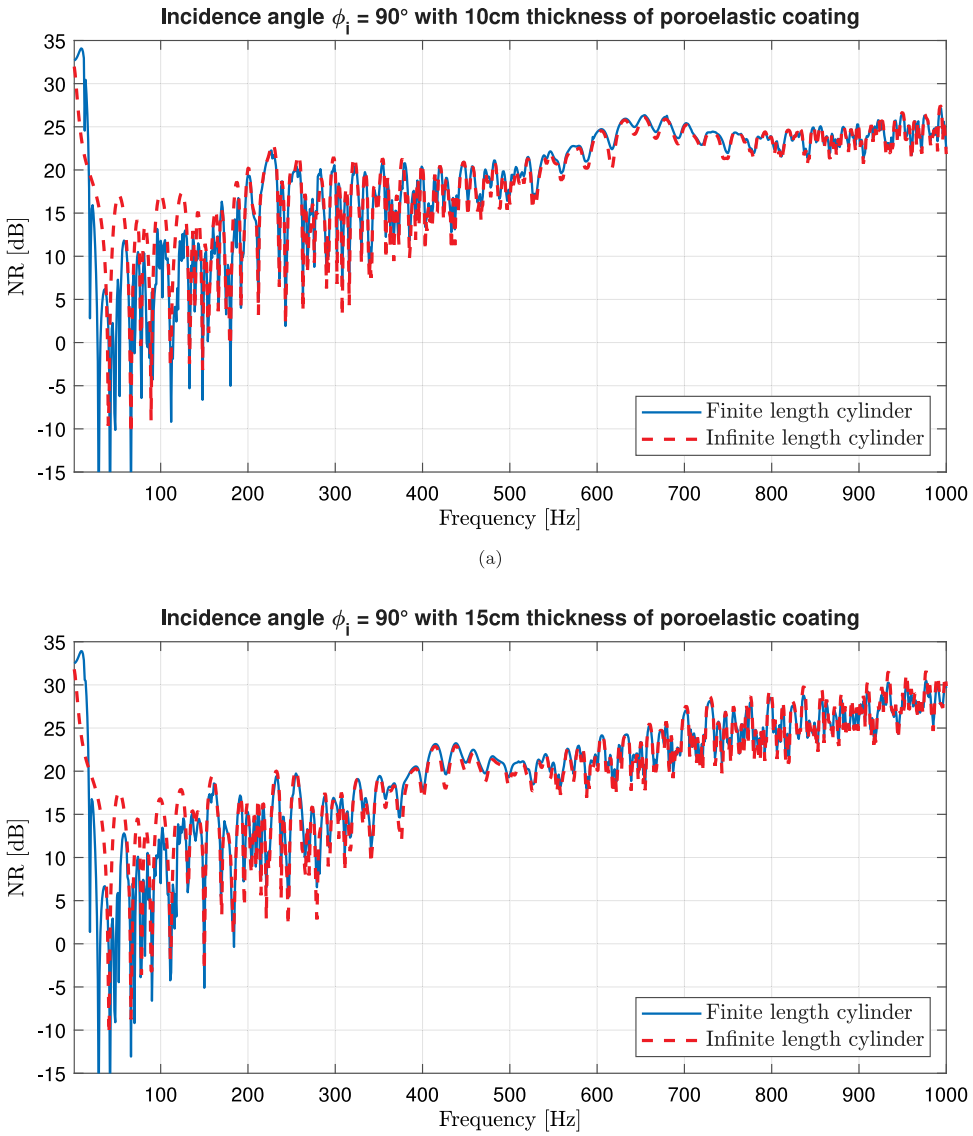

Fig. 13. Noise reduction superposition of finite length cylinder (proposed model) and infinite length cylinder (reference [13]) excited by a plane wave with normal incidence $\phi_i = 90^\circ$. (a) Shell lined with 10 cm thickness of poroelastic coating (b) Shell lined with 15 cm thickness of poroelastic coating.

Table 2
Sandwich shell properties.

Properties		Skin	Core
Thickness	[mm]	0.858	18.2
Mass density	[kg/m^3]	3 288.5	136.153 8
Young modulus E_z	[GPa]	53.877	0
Young modulus E_θ	[GPa]	17.475	0
Shear modulus $G_{z\theta}$	[GPa]	7.8	0
Shear modulus G_{zr}	[GPa]	0	0.186 2
Shear modulus $G_{\theta r}$	[GPa]	0	0.089 6
Poisson ratio $\nu_{z\theta}$		0.594	0
Structural damping η	[%]	1	1

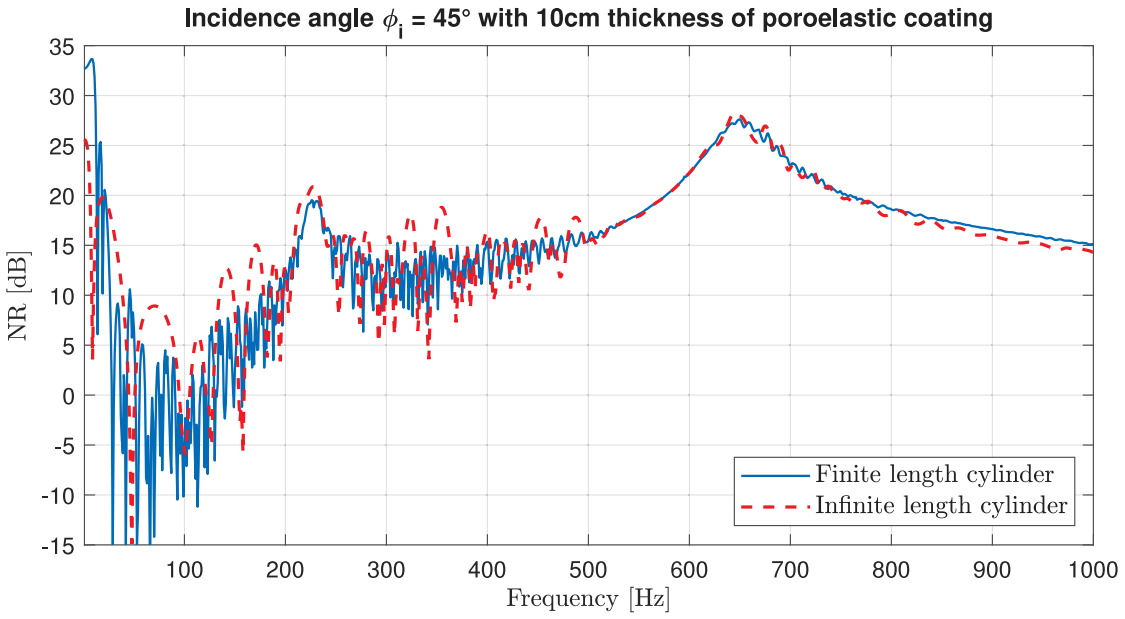

(a)

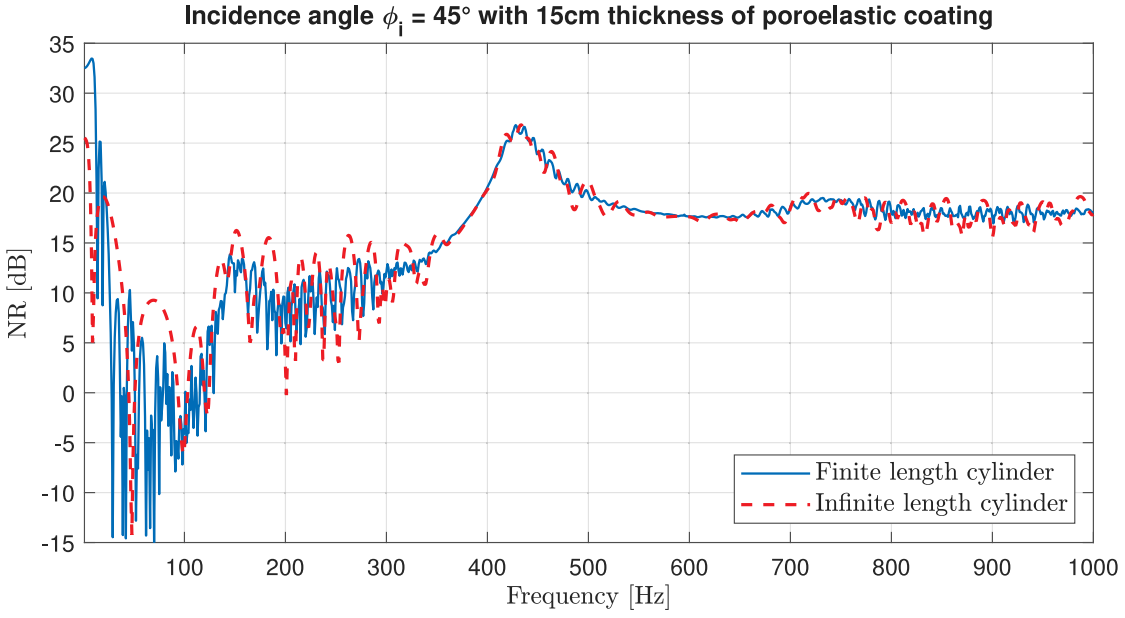

(b)

Fig. 14. Noise reduction superposition of finite length cylinder (proposed model) and infinite length cylinder (reference [13]) excited by a plane wave with incidence $\phi_i = 45^\circ$. (a) Shell lined with 10 cm thickness of poroelastic coating (b) Shell lined with 15 cm thickness of poroelastic coating.

Results obtained for naked cylinders are compared and validated with results from literature and those obtained with full numerical FEM–BEM approach. Besides, the present model is put into perspective through finite/infinite results juxtaposition and the internal resonances brought by the finitude of the cylinder are discussed with respect to angle of incidence and poroelastic coating thickness in the low and mid frequency ranges. The main observations are summarized hereafter. It is found that the effects of the boundary conditions are limited to the very first low frequency range where there are large discrepancies between finite and infinite Noise Reduction (NR) levels for both naked and coated cylinder configurations. Despite this difference, the finite and infinite cylinder results are in a very good agreement for normal incidence where the NR fluctuations are matching well.

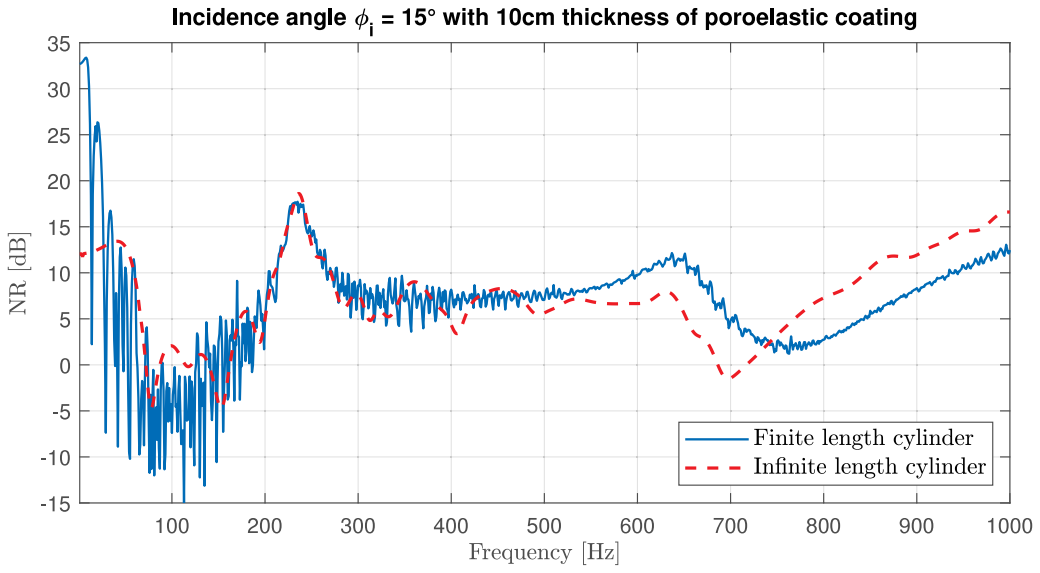

(a)

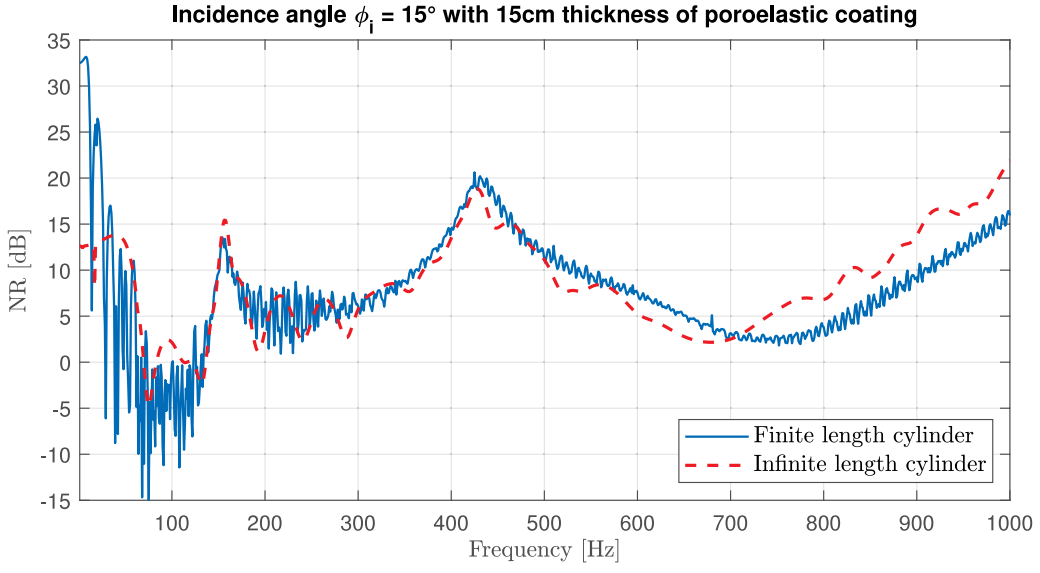

(b)

Fig. 15. Noise reduction superposition of finite length cylinder (proposed model) and infinite length cylinder (reference [13]) excited by a plane wave with incidence $\phi_i = 15^\circ$. (a) Shell lined with 10 cm thickness of poroelastic coating (b) Shell lined with 15 cm thickness of poroelastic coating.

However, for oblique incidence and for naked cylinders, the NR curve obtained by the infinite model is more regular with less fluctuations while the NR curve obtained by the proposed model is still fluctuating due to the effects of the internal resonances. Globally speaking, both models are in a good agreement with a general relative NR level overestimation observed for infinite cylinder.

For coated cylinders, it is found that the poroelastic liner does not improve sound insulation in the stiffness controlled region and this is explained by its high flexibility. However, in the mass controlled region, the sound insulation is greatly improved thanks to the viscous and thermal dissipation and the effects of finite cylinder internal resonances are muffled. For highly oblique incidences, a gap between finite and infinite is found. Finally, unlike infinite length cylinder model, the proposed finite length cylinder model presents all the structural and acoustical resonances for a more accurate sound level transmission prediction.

Table 3
Properties of the poroelastic material and the interstitial fluid.

Properties		Value
Porosity ϕ		0.994
Tortuosity α_∞		1.02
Flow resistivity σ	[N s m^{-4}]	9 045
Viscous characteristic length Λ	[μm]	103
Thermal characteristic length Λ'	[μm]	197
Skeleton mass density ρ_{1s}	[kg/m^3]	8.43
Skeleton first Lamé parameter λ	[kPa]	360.2905
Skeleton second Lamé parameter μ	[kPa]	68.6268
Skeleton structural damping η_s	[%]	5
Fluid mass density ρ_f	[kg/m^3]	1.284
Fluid dynamic viscosity η_f	[μPa s]	18.4
Fluid heat capacity ratio γ_f		1.4
Prandtl number Pr		0.71
Atmospheric pressure P_0	[Pa]	101 325

CRediT authorship contribution statement

Fares Naccache: Conceptualization, Methodology, Investigation, Validation, Software, Writing – original draft, Writing – review & editing. **Mohamed-Ali Hamdi:** Conceptualization, Methodology, Validation, Writing – original draft, Writing – review & editing, Supervision, Funding acquisition. **Jean-Daniel Chazot:** Methodology, Validation, Writing – review & editing, Resources. **Marc Anciant:** Validation, Writing – review & editing.

Declaration of competing interest

The authors declare that they have no known competing financial interests or personal relationships that could have appeared to influence the work reported in this paper.

Acknowledgments

This work was carried out with the financial support of ArianeGroup and the french National Centre for Space Studies (Centre National d'Études Spatiales - CNES). The authors express their sincere thank and acknowledgment for this support.

Appendix A. Shell properties

For an K-layered laminated shell made of transversely isotropic materials, the generalized stiffness coefficients $\left(A_{ij}, \bar{A}_{ij}, \hat{A}_{ij}\right)$, $\left(D_{ij}, \bar{D}_{ij}, \hat{D}_{ij}\right)$ and $\left(B_{ij}, \bar{B}_{ij}, \hat{B}_{ij}\right)$ represent respectively the extensional, bending and extensional-bending coupling stiffness coefficients and are evaluated as follows:

$$A_{ij} = \sum_{k=1}^{K} Q_{ij}^{(k)} \left(h_k - h_{k-1}\right) \qquad i,j = 1,2,6 \tag{A.1a}$$

$$B_{ij} = \frac{1}{2} \sum_{k=1}^{K} Q_{ij}^{(k)} \left(h_k^2 - h_{k-1}^2\right) \qquad i,j = 1,2,6 \tag{A.1b}$$

$$D_{ij} = \frac{1}{3} \sum_{k=1}^{K} Q_{ij}^{(k)} \left(h_k^3 - h_{k-1}^3\right) \qquad i,j = 1,2,6 \tag{A.1c}$$

$$E_{ij} = \frac{1}{4} \sum_{k=1}^{K} Q_{ij}^{(k)} \left(h_k^4 - h_{k-1}^4\right) \qquad i,j = 1,2,6 \tag{A.1d}$$

$$A_{ij} = C \sum_{k=1}^{K} Q_{ij}^{(k)} \left(h_k - h_{k-1}\right) \qquad i,j = 4,5 \tag{A.1e}$$

$$B_{ij} = C \frac{1}{2} \sum_{k=1}^{K} Q_{ij}^{(k)} \left(h_k^2 - h_{k-1}^2\right) \qquad i,j = 4,5 \tag{A.1f}$$

$$\bar{A}_{ij} = A_{ij} + \frac{B_{ij}}{R_m} \qquad \hat{A}_{ij} = A_{ij} - \frac{B_{ij}}{R_m} \tag{A.1g}$$

$$\bar{B}_{ij} = B_{ij} + \frac{D_{ij}}{R_m} \qquad \hat{B}_{ij} = B_{ij} - \frac{D_{ij}}{R_m} \tag{A.1h}$$

$$\bar{D}_{ij} = D_{ij} + \frac{E_{ij}}{R_m} \qquad \hat{D}_{ij} = D_{ij} - \frac{E_{ij}}{R_m} \tag{A.1i}$$

where h_k, h_{k-1} are the distance from the midsurface to the outer and inner surfaces of the kth layer respectively, $\bar{Q}_{ij}^{(k)}$ are the plane-stress reduced stiffness coefficients of the kth cross-ply lamina and given in terms of elastic properties and $C = \frac{5}{6}$ the shear correction factor.

For each lamina layer k, the *reduced* Hooke law for transversely isotropic materials is given by:

$$Q_{11}^{(k)} = \frac{E_z^{(k)}}{1 - \nu_{z\theta}^{(k)} \nu_{\theta z}^{(k)}} \qquad Q_{22}^{(k)} = \frac{E_\theta^{(k)}}{1 - \nu_{z\theta}^{(k)} \nu_{z\theta}^{(k)}} \tag{A.2a}$$

$$Q_{12}^{(k)} = \frac{\nu_{\theta z}^{(k)} E_z^{(k)}}{1 - \nu_{z\theta}^{(k)} \nu_{\theta z}^{(k)}} \qquad Q_{21}^{(k)} = \frac{\nu_{z\theta}^{(k)} E_\theta^{(k)}}{1 - \nu_{z\theta}^{(k)} \nu_{\theta z}^{(k)}} \tag{A.2b}$$

$$Q_{44}^{(k)} = G_{r\theta}^{(k)} \qquad Q_{55}^{(k)} = G_{zr}^{(k)} \qquad Q_{66}^{(k)} = G_{\theta z}^{(k)} \tag{A.2c}$$

with $\left(E_z, E_\theta\right)$ the Young moduli in longitudinal and transverse fiber directions respectively, $\left(\nu_{z\theta}, \nu_{\theta z}\right)$ the Poisson coefficients and $\left(G_{r\theta}, G_{zr}, G_{\theta z}\right)$ the shear moduli. These relationships are valid when the lamina principle axes coincide with the cylindrical axes.

The inertial coefficients are given by:

$$\bar{I}_i = I_i + \frac{I_{i+1}}{R_m} \qquad i = 1, 2, 3 \tag{A.3a}$$

$$\left[I_1, I_2, I_3, I_4\right] = \sum_{k=1}^{K} \int_{h_{k-1}}^{h_k} \rho^{(k)} \left[1, r, r^2, r^3\right] \, r dr \tag{A.3b}$$

where $\rho^{(k)}$ denotes the density of the kth laminated layer.

Appendix B. Biot's parameters

For harmonic motion $\left(e^{-\mathrm{j}\omega t}\right)$, the effective densities introduced in the mixed displacement–pressure Biot formulation Eq. (20) and Eq. (22) are defined as follows:

$$\tilde{\rho}_{11} = \rho_{11} - \frac{\tilde{b}}{\mathrm{j}\omega} \tag{B.1a}$$

$$\tilde{\rho}_{22} = \rho_{22} - \frac{\tilde{b}}{\mathrm{j}\omega} \tag{B.1b}$$

$$\tilde{\rho}_{12} = \rho_{12} + \frac{\tilde{b}}{\mathrm{j}\omega} \tag{B.1c}$$

$$\tilde{\rho} = \tilde{\rho}_{11} - \frac{\tilde{\rho}_{12}^2}{\tilde{\rho}_{22}} \tag{B.1d}$$

where ρ_{11} and ρ_{22} are skeleton and fluid mass coefficients respectively, ρ_{12} mass coefficient accounting for inertial interaction between solid and fluid phases. These coefficients are expressed in terms of skeleton mass density ρ_s and interstitial fluid density ρ_f:

$$\rho_{11} = (1 - \phi)\, \rho_s - \rho_{12} \tag{B.2a}$$

$$\rho_{22} = \alpha_\infty \phi \rho_f \tag{B.2b}$$

$$\rho_{12} = \left(1 - \alpha_\infty\right) \phi \rho_f \tag{B.2c}$$

The viscous damping coefficient $\tilde{b}$ is dependent on the frequency and it is expressed using the Johnson and al.[44] model.

The elastic and inertial coupling coefficients α and β between solid and fluid phases are given by [41]:

$$\alpha = 1 + \frac{\tilde{Q}}{\tilde{R}} \tag{B.3a}$$

$$\beta = 1 + \frac{\tilde{\rho}_{12}}{\tilde{\rho}_{22}} \tag{B.3b}$$

where $\tilde{Q}$ and $\tilde{R}$ are elastic coefficient related to the bulk moduli of skeleton and interstitial fluid.

References

[1] M. Biot, Theory of elastic waves in a fluid-saturated porous solid. 1. Low frequency range, J. Acoust. Soc. Am. 28 (1956) 168–178, http://dx.doi.org/10.1121/1.1908239.

[2] M.A. Biot, Theory of propagation of elastic waves in a fluid-saturated porous solid. 2. Higher frequency range, J. Acoust. Soc. Am. 28 (2) (1956) 179–191, http://dx.doi.org/10.1121/1.1908241.

[3] J.-H. Lee, J. Kim, H.-J. Kim, Simplified method to solve sound transmission through structures lined with elastic porous material, J. Acoust. Soc. Am. 110 (5) (2001) 2282–2294, http://dx.doi.org/10.1121/1.1410967.

[4] J. Bolton, N.-M. Shiau, Y. Kang, Sound transmission through multi-panel structures lined with elastic porous materials, J. Sound Vib. 191 (3) (1996) 317–347, http://dx.doi.org/10.1006/jsvi.1996.0125.

[5] J. Zhou, A. Bhaskar, X. Zhang, The effect of external mean flow on sound transmission through double-walled cylindrical shells lined with poroelastic material, J. Sound Vib. 333 (7) (2014) 1972–1990, http://dx.doi.org/10.1016/j.jsv.2013.11.038.

[6] Y. Liu, C. He, Diffuse field sound transmission through sandwich composite cylindrical shells with poroelastic core and external mean flow, Compos. Struct. 135 (2016) 383–396, http://dx.doi.org/10.1016/j.compstruct.2015.09.025.

[7] M. Golzari, A.A. Jafari, Sound transmission loss through triple-walled cylindrical shells with porous layers, J. Acoust. Soc. Am. 143 (6) (2018) 3529–3544, http://dx.doi.org/10.1121/1.5041270.

[8] K. Daneshjou, H. Ramezani, R. Talebitooti, Wave transmission through laminated composite double-walled cylindrical shell lined with porous materials, Appl. Math. Mech. 32 (6) (2011) 701–718, http://dx.doi.org/10.1007/s10483-011-1450-9.

[9] J. Zhou, A. Bhaskar, X. Zhang, Sound transmission through a double-panel construction lined with poroelastic material in the presence of mean flow, J. Sound Vib. 332 (16) (2013) 3724–3734, http://dx.doi.org/10.1016/j.jsv.2013.02.020.

[10] K. Daneshjou, R. Talebitooti, M. Kornokar, Vibroacoustic study on a multilayered functionally graded cylindrical shell with poroelastic core and bonded-unbonded configuration, J. Sound Vib. 393 (2017) 157–175, http://dx.doi.org/10.1016/j.jsv.2017.01.001.

[11] R. Talebitooti, M. Zarastvand, The effect of nature of porous material on diffuse field acoustic transmission of the sandwich aerospace composite doubly curved shell, Aerosp. Sci. Technol. 78 (2018) 157–170, http://dx.doi.org/10.1016/j.ast.2018.03.010.

[12] R. Talebitooti, A. Choudari Khameneh, M. Zarastvand, M. Kornokar, Investigation of three-dimensional theory on sound transmission through compressed poroelastic sandwich cylindrical shell in various boundary configurations, J. Sandw. Struct. Mater. 21 (7) (2019) 2313–2357, http://dx.doi.org/10.1177/1099636217751562.

[13] J. Magniez, M.A. Hamdi, J.-D. Chazot, B. Troclet, A mixed "Biot-shell" analytical model for the prediction of sound transmission through a sandwich cylinder with a poroelastic core, J. Sound Vib. 360 (2016) 203–223, http://dx.doi.org/10.1016/j.jsv.2015.09.012.

[14] M. Zarastvand, M. Ghassabi, R. Talebitooti, Acoustic insulation characteristics of shell structures: a review, Arch. Comput. Methods Eng. 28 (2) (2021) 505–523, http://dx.doi.org/10.1177/1099636221993891.

[15] J. Magniez, J.-D. Chazot, M.A. Hamdi, B. Troclet, A mixed 3D-shell analytical model for the prediction of sound transmission through sandwich cylinders, J. Sound Vib. 333 (19) (2014) 4750–4770, http://dx.doi.org/10.1016/j.jsv.2014.04.040.

[16] L. Tong, Free vibration of orthotropic conical shells, Int. J. Eng. Sci. 31 (5) (1993) 719–733, http://dx.doi.org/10.1016/0020-7225(93)90120-J.

[17] M. Caresta, N.J. Kessissoglou, Free vibrational characteristics of isotropic coupled cylindrical–conical shells, J. Sound Vib. 329 (6) (2010) 733–751, http://dx.doi.org/10.1016/j.jsv.2009.10.003.

[18] M. Caresta, N.J. Kessissoglou, Acoustic signature of a submarine hull under harmonic excitation, Appl. Acoust. 71 (1) (2010) 17–31, http://dx.doi.org/10.1016/j.apacoust.2009.07.008.

[19] M. Golzari, A.A. Jafari, Sound transmission through truncated conical shells, Appl. Acoust. 156 (2019) 186–207, http://dx.doi.org/10.1016/j.apacoust.2019.07.008.

[20] H. Darvish Gohari, M. Zarastvand, R. Talebitooti, Acoustic performance prediction of a multilayered finite cylinder equipped with porous foam media, J. Vib. Control 26 (11–12) (2020) 899–912, http://dx.doi.org/10.1177/1077546319890025.

[21] V. Easwaran, W. Lauriks, J. Coyette, Displacement-based finite element method for guided wave propagation problems: Application to poroelastic media, J. Acoust. Soc. Am. 100 (5) (1996) 2989–3002, http://dx.doi.org/10.1121/1.417111.

[22] Y.J. Kang, B.K. Gardner, J.S. Bolton, An axisymmetric poroelastic finite element formulation, J. Acoust. Soc. Am. 106 (2) (1999) 565–574, http://dx.doi.org/10.1121/1.428041.

[23] M.J. Kingan, Y. Yang, B.R. Mace, Sound transmission through cylindrical structures using a wave and finite element method, Wave Motion 87 (2019) 58–74, http://dx.doi.org/10.1016/j.wavemoti.2018.07.009.

[24] H. Li, Y. Hao, W. Zhang, L. Liu, S. Yang, D. Wang, Vibration analysis of porous metal foam truncated conical shells with general boundary conditions using GDQ, Comput. Struct. 269 (2021) 114036, http://dx.doi.org/10.1016/j.compstruct.2021.114036.

[25] F.J. Fahy, Statistical energy analysis: A critical overview, Philos. Trans. R. Soc. Lond. Ser. A: Phys. Eng. Sci. 346 (1681) (1994) 431–447, http://dx.doi.org/10.1098/rsta.1994.0027.

[26] P.H. White, Sound transmission through a finite, closed, cylindrical shell, J. Acoust. Soc. Am. 40 (5) (1966) 1124–1130, http://dx.doi.org/10.1121/1.1910197.

[27] L.D. Pope, On the transmission of sound through finite closed shells: Statistical energy analysis, modal coupling, and nonresonant transmission, J. Acoust. Soc. Am. 50 (3B) (1971) 1004–1018, http://dx.doi.org/10.1121/1.1912694.

[28] C. Yuan, O. Bergsma, A. Beukers, Sound transmission loss prediction of the composite fuselage with different methods, Appl. Comp. Mater. 19 (6) (2012) 865–883, http://dx.doi.org/10.1007/s10443-011-9199-6.

[29] P. Oliazadeh, A. Farshidianfar, M.J. Crocker, Experimental and analytical investigation on sound transmission loss of cylindrical shells with absorbing material, J. Sound Vib. 434 (2018) 28–43, http://dx.doi.org/10.1016/j.jsv.2018.07.017.

[30] P. Gupta, A. Parey, Prediction of sound transmission loss of cylindrical acoustic enclosure using statistical energy analysis and its experimental validation, J. Acoust. Soc. Am. 151 (1) (2022) 544–560, http://dx.doi.org/10.1121/10.0009358.

[31] J.-H. Lee, J. Kim, Study on sound transmission characteristics of a cylindrical shell using analytical and experimental models, Appl. Acoust. 64 (6) (2003) 611–632, http://dx.doi.org/10.1016/S0003-682X(02)00138-X.

[32] L.R. Koval, Effects of cavity resonances on sound transmission into a thin cylindrical shell, J. Sound Vib. 59 (1) (1978) 23–33, http://dx.doi.org/10.1016/0022-460X(78)90475-3.

[33] C. Lesueur, Rayonnement Acoustique Des Structures: Vibroacoustique, Interaction Fluide-Structure (in French) [Sound Radiation of Structures : Vibroacoustics, Fluid-Structure Interaction], Eyrolles, 1988.

[34] D. Li, J.S. Vipperman, Mathematical model for characterizing noise transmission into finite cylindrical structures, J. Acoust. Soc. Am. 117 (2) (2005) 679–689, http://dx.doi.org/10.1121/1.1828652.

[35] H. Hosseini-Toudeshky, M. Mofakhami, S.H. Hashemi, Sound transmission into a thick hollow cylinder with the fixed-end boundary condition, Appl. Math. Model. 33 (3) (2009) 1656–1673, http://dx.doi.org/10.1016/j.apm.2008.03.002.

[36] M. Mofakhami, H.H. Toudeshky, S.H. Hashemi, Finite cylinder vibrations with different end boundary conditions, J. Sound Vib. 297 (1–2) (2006) 293–314, http://dx.doi.org/10.1016/j.jsv.2006.03.041.

[37] J. Zhou, A. Bhaskar, X. Zhang, Sound transmission through double cylindrical shells lined with porous material under turbulent boundary layer excitation, J. Sound Vib. 357 (2015) 253–268, http://dx.doi.org/10.1016/j.jsv.2015.07.014.
[38] M. Golzari, A.A. Jafari, Effect of poroelastic material on vibroacoustic behavior of truncated conical shells, Aerosp. Sci. Technol. 118 (2021) 106982, http://dx.doi.org/10.1016/j.ast.2021.106982.
[39] M.S. Qatu, Vibration of Laminated Shells and Plates, Elsevier, 2004.
[40] J.N. Reddy, Mechanics of Laminated Composite Plates and Shells: Theory and Analysis, CRC Press, 2003.
[41] J. Allard, N. Atalla, Propagation of Sound in Porous Media: Modelling Sound Absorbing Materials 2e, John Wiley & Sons, 2009.
[42] M. Hamdi, L. Mebarek, A. Omrani, N. Atalla, An efficient formulation for the analysis of acoustic and elastic waves propagation in porous-elastic materials, in: Proceedings of the International Seminar on Modal Analysis, Vol. 3, Katholieke Universiteit Leuven, Belgium, 2001, pp. 1443–1448, https://www.jstor.org/stable/44731003.
[43] N. Atalla, M.A. Hamdi, R. Panneton, Enhanced weak integral formulation for the mixed (u_, p_) poroelastic equations, J. Acoust. Soc. Am. 109 (6) (2001) 3065–3068, http://dx.doi.org/10.1121/1.1365423.
[44] D.L. Johnson, J. Koplik, R. Dashen, Theory of dynamic permeability and tortuosity in fluid-saturated porous media, J. Fluid Mech. 176 (1987) 379–402, http://dx.doi.org/10.1017/S0022112087000727.
[45] Y. Champoux, J.-F. Allard, Dynamic tortuosity and bulk modulus in air-saturated porous media, J. Appl. Phys. 70 (4) (1991) 1975–1979, http://dx.doi.org/10.1063/1.349482.
[46] P. Oliazadeh, A. Farshidianfar, Analysis of different techniques to improve sound transmission loss in cylindrical shells, J. Sound Vib. 389 (2017) 276–291, http://dx.doi.org/10.1016/j.jsv.2016.11.016.
[47] A. Blaise, C. Lesueur, M. Gotteland, M. Barbe, On sound transmission into an orthotropic infinite shell: Comparison with Koval's results and understanding of phenomena, J. Sound Vib. 150 (2) (1991) 233–243, http://dx.doi.org/10.1016/0022-460X(91)90618-T.
[48] P. Smith Jr., Sound transmission through thin cylindrical shells, J. Acoust. Soc. Am. 29 (6) (1957) 721–729, http://dx.doi.org/10.1121/1.1909025.
[49] F. Xin, T. Lu, C. Chen, Vibroacoustic behavior of clamp mounted double-panel partition with enclosure air cavity, J. Acoust. Soc. Am. 124 (6) (2008) 3604–3612, http://dx.doi.org/10.1121/1.3006956.
[50] F. Xin, T. Lu, Analytical modeling of sound transmission through clamped triple-panel partition separated by enclosed air cavities, Europ. J. Mech.-A/Solids 30 (6) (2011) 770–782, http://dx.doi.org/10.1016/j.euromechsol.2011.04.013.